Inorganic Chemistry Communications 179 (2025) 114876

Contents lists available at ScienceDirect

Inorganic Chemistry Communications

journal homepage: www.elsevier.com/locate/inoche

Research Article

Crystal structure, spectroscopic investigation (FT-IR, NMR, and UV–Vis), DFT calculations, and in vitro antioxidant, α-glucosidase, and α-amylase inhibitor activity determination of the ethyl 1H-imidazole-1-carboxylate molecule and its new synthesized silver perchlorate complex

Ceyhun Kucuk [a,*], Meltem Erdem-Kucuk [a], Ebru Coteli [b], Sibel Celik [b], Namık Özdemir [c]

[a] Ahmet Erdogan Vocational School of Health Services, Zonguldak Bulent Ecevit University, 67600 Zonguldak, Turkey
[b] Vocational School of Health Services, Kırsehir Ahi Evran University, 40100 Kırşehir, Turkey
[c] Department of Physics, Faculty of Science, Ondokuz Mayıs University, 55139 Samsun, Turkey

ARTICLE INFO

Keywords:
1H-imidazole
DFT
Silver perchlorate
Biological activity

ABSTRACT

In this study, spectroscopic characterizations (FT-IR, UV–Vis, and NMR) of the ethyl 1H-imidazole-1-carboxylate (EIMC) ligand and the new synthesized $[Ag(EIMC)_2]ClO_4$ complex were performed. Also, the electronic, optical, and biological activity properties of these compounds were investigated. First of all, the EIMC ligand and $[Ag(EIMC)_2]ClO_4$ complex were optimized by using suitable basis sets. The theoretical equivalent values of the data in the experimental FT-IR spectrum were calculated for the optimized structures, and it was determined that the theoretical values were in agreement with the experimental results. The spectroscopic characterization stage was completed by recording NMR and UV–Vis spectra and performing theoretical calculations. The energy gap value between the HOMO and LUMO orbitals was found to be 5.66 and 5.08 eV for the free ligand and the synthesized Ag (I) complex. The molecular electrostatic potential maps, electron localization function (ELF) and localized orbital locator (LOL) maps, atomic polar tensor (APT), Hirshfeld, and natural bond orbital (NBO) charge analyses, and Fukui functions were calculated for the gas phase. Experimental results regarding antioxidant and antidiabetic activity showed that especially the ligand had the highest radical scavenging ($DPPH^{\bullet}$ IC_{50} = 103.36 μg/mL) and the complex had the highest α-glucosidase (IC_{50} = 156.12 μg/mL) enzyme inhibition.

1. Introduction

Imidazole is a planar heterocyclic ring consisting of five members, with three carbon and two nitrogen atoms. The ring contains nitrogen in the first and third positions [1]. Various significant natural substances, including purine, histamine, histidine, and nucleic acid, contain the imidazole ring as a component [2,3]. As a polar aromatic chemical, it is easily soluble in water [1]. Imidazole derivatives hold a distinct and significant position in the realm of medicinal chemistry. The discipline of medicinal chemistry benefits greatly from the wide range of synthetic techniques available for imidazole and its diverse structural reactions. Imidazole medications have expanded their range of applications in treating numerous conditions in clinical medicine. Medical chemists have been motivated to create several new chemotherapeutic medicines because of the significant therapeutic effects of imidazole-related medications [4]. The medicinal properties of imidazole encompass a wide range of effects, including its ability to inhibit cancer growth, β-lactamase enzymes, and the synthesis of 20-Hydroxy-5,8,11,14-eicosatetraenoic acid [5]. Imidazole also acts as an inhibitor for carboxypeptidase and hemeoxygenase enzymes, making it useful in various therapeutic applications. Imidazole-based hybrids display a wide range of bioactivities due to their ability to effectively bind to various enzymes and receptors in biological systems through weak interactions such as hydrogen bonds, ion dipoles, cation-π interactions, π-π stacking, coordination, Van der Waals forces, and hydrophobic effects. Additionally, imidazole exhibits anti-aging properties and functions as an anticoagulant, anti-inflammatory, antibacterial, antifungal, antiviral, antitubercular, antidiabetic, and antimalarial agent [6–8]. Since the drugs that prevent diabetes have limited [9] and side effects, the discovery of drug substances with fewer side effects is of vital importance [10]. The silver

* Corresponding author.
E-mail address: ceyhun.kucuk@beun.edu.tr (C. Kucuk).

https://doi.org/10.1016/j.inoche.2025.114876
Received 13 May 2025; Received in revised form 4 June 2025; Accepted 9 June 2025
Available online 13 June 2025
1387-7003/© 2025 Elsevier B.V. All rights are reserved, including those for text and data mining, AI training, and similar technologies.

element is a catalytic agent that effectively catalyzes reduction reactions [11,12]. This atom shows high biological activity even at low doses. It has many activities, such as inhibiting cellular respiration, binding nucleic acids, damaging cell membranes, and binding thiols in the structure of proteins and enzymes [13]. It has also been reported that the silver (I) element has important pharmacological activities such as antibacterial, anti-ulcer, and antifungal [14–16], antitumor [17,18], and anticancer agents [14,15]. Therefore, complexes synthesized with silver have an important place in pharmacology. In other studies, it has been reported that transition metal complexes have many biological activities, such as anti-inflammatory, anti-cancer, antidiabetic, and antibacterial [19,20]. Substances that are willing to enter into chemical reactions, have unpaired electrons in their last orbitals, have high energy, and are unstable are called free radicals [21,22]. These radicals cause oxidative damage to the plasma membrane, leading to the development of important diseases such as cancer, coronary vascular diseases, and diabetes. In particular, experimental studies have indicated that diabetes is associated with reactive oxygen species (ROS) [23,24,25]. Recently, there has been a significant increase in diabetes due to hyperlipidemia, smoking, unhealthy diet, and aging [26]. Diabetes mellitus is a metabolic disorder that occurs when blood glucose levels increase after meals and is called hyperglycemia. This metabolic disorder leads to many disorders, such as cardiovascular diseases, nerve damage, kidney failure, blindness, and nerve damage [27–29]. Computational methods have been used frequently to elucidate and predict molecular-level behavior [30]. Density functional theory (DFT) has become one of the most widely used tools today because it can accurately determine the energy of a molecule and simulate chemical processes using quantum mechanical calculation methods [31]. Using DFT calculations, researchers can obtain the geometric structure of organic or inorganic molecules in their most stable ground state energy, define reaction mechanisms, and determine reactive regions by characterizing their electronic properties. Additionally, spectroscopic characterization calculations such as IR, Raman, NMR, and UV–Vis can also be performed [32].

In the first part of this study, spectroscopic characterizations of the EIMC ligand and $[Ag(EIMC)_2]ClO_4$ complex were performed by recording FT-IR, NMR, and UV–Vis spectra. Additionally, theoretical values will be obtained through DFT calculations and combined with experimental values. In the second part of the study, the energy values of the highest occupied molecular orbital (HOMO) and the lowest empty molecular orbital (LUMO), the energy gap value between these two orbitals, and the spherical hardness and chemical potential values will be determined in the gas phase to obtain information about the chemical reactivity of the title molecule. Additionally, to determine the reactive regions of the EIMC ligand and the $[Ag(EIMC)_2]ClO_4$ complex, molecular electrostatic potential (MEP), ELF, and LOL maps will be created, and charge values and Fukui functions will be calculated. In the last section, in vitro antioxidant, α-glucosidase, and α-amylase inhibitory activity studies will be carried out to investigate the biological activities of both structures due to the reasons mentioned above. The final focus of this study is to synthesize a new Ag(I) complex from the EIMC ligand, to obtain the geometric structure of the synthesized complex by performing spectroscopic characterization of both structures, to investigate the electronic properties of these two structures to determine their reactivity, and to evaluate the antioxidant, α-glucosidase, and α-amylase activities.

2. Materials and methods

2.1. Computational methods

Structural, spectroscopic, electronic, and optical properties were calculated with the Gaussian 16 W package program [33], and images were designed with the GaussView 6.1 program [34]. Except for ^{1}H and ^{13}C NMR calculations, all other calculations were performed using the B3LYP functional and 6–311++G(d,p) basis set in density functional theory (DFT) for the EIMC ligand [35,36]. NMR calculations were carried out using the same theory and functional in the DMSO solvent in the IEFPCM model and the 6–311 + G(2d,p) basis set [37]. Optimization, spectroscopic, electronic, and optical property calculations for the $[Ag(EIMC)_2]ClO_4$ complex were performed at the DFT/B3LYP/6–311++G(d,p) + DGDZVP level of theory [38]. Also, ^{1}H and ^{13}C NMR calculations were carried out using the DFT/B3LYP/6–311 + G(2d,p) + DGDZVP theory level in IEFPCM modeled DMSO solvent [39]. UV–Vis calculations were performed by selecting water as the solvent in the IEFPCM model with the same method used in the calculation of electronic properties for both structures [40]. The Multiwfn program was used to generate ELF and LOL surface maps and reduced density gradient (RDG) analysis [41]. Hirshfeld surfaces were mapped and two-dimensional fingerprint diagrams were generated using the Crystal Explorer 17 tool [42–44].

2.2. Experimental analyses

2.2.1. Synthesis and recording of spectra

Ethyl 1H-imidazole-1-carboxylate (EIMC) (97 % purity) and silver perchlorate $AgClO_4$ (97 % purity) were obtained from BLDpharm and Sigma Aldrich Chemical Company, respectively. In the synthesis phase, solutions were prepared in ethanol (98 % purity) for the EIMC ligand and $AgClO_4$ without an additional purification process. In the first stage, a 2 mmol EIMC solution was prepared in 10 ml of ethanol and mixed with a magnetic stirrer for 5 min at 30 °C. In the second stage, a 1 mmol $AgClO_4$ solution was prepared in 10 ml of ethanol and mixed for 5 min at 30 °C. Finally, the prepared $AgNO_3$ solution was added dropwise to the EIMC solution, stirred at 30 °C for 60 min, and a white precipitate was obtained. The resulting precipitate was filtered using filter paper and a funnel. The remaining solution was left at room temperature for approximately 30 days to get the single crystal structure of the synthesized complex, and the single crystal structure of the $[Ag(EIMC)_2]ClO_4$ was obtained.

The FT-IR spectra were recorded between 4000 and 400 cm^{-1} using a Bruker FT-IR spectrometer with ATR equipment. ^{1}H NMR and ^{13}C NMR spectra were recorded in the range of 0–15 ppm and 100–200 ppm, respectively, in DMSO solvent using a Bruker Avance NEO 500 Nuclear Magnetic Resonance Spectrometer. The UV–Vis spectrum was recorded in the range of 190–1100 nm using the T80 + UV/Vis spectrometer.

2.2.2. Determination of antioxidant activity

2.2.2.1. $ABTS^{\bullet+}$ radical scavenging activity. The ability of ligand, complex, and standard substance samples to scavenge free radicals was measured using $ABTS^{\bullet+}$ [2,2′-Azino-bis(3-ethylbenzthiazoline-6-sulfonic acid)] radical [45]. 7 mM ABTS and 2.45 mM $Na_2S_2O_8$ solutions were prepared and combined in the ratio (1:0.5). This mixture was stirred in the dark for 16 h. The absorbance of the resulting radical mixture at 734 nm wavelength was adjusted to 0.7 by diluting with ethanol solution (80 %). Ascorbic acid was used as a standard substance. 50 μL of the samples prepared at concentrations of 25, 50, and 100 μg/

mL were taken and combined with 2 mL of radical solution. The absorbance values of the samples kept in the dark for 30 min were determined at 734 nm. The same procedures were applied by adding ethanol to the control tube instead of the sample. The radical inhibition values of all samples in the study were calculated using the equation below. In addition, IC_{50} (inhibitory concentration) values were determined using the % inhibition values.

$$\%\boldsymbol{inhibisyonofradicals}(\boldsymbol{ABTS^{+}}) = \frac{(\boldsymbol{ControlAbs} - \boldsymbol{Sample/StandartAbs})}{\boldsymbol{ControlAbs}}\boldsymbol{x}100 \quad (1)$$

2.2.2.2. DPPH• radical scavenging activity. Radical scavenging activity of the samples in the study was determined using DPPH• (2,2-diphenyl-1-picrylhydrazyl) [46]. Samples were prepared from the ligand, complex, and standard ascorbic acid substances in the study at concentrations of 25, 50, and 100 μg/mL. A 0.1 mM DPPH radical solution was prepared in methanol. 0.5 mL was taken from the samples in the study and combined with 2 mL of radical solution. The absorbances of the samples kept in the dark for 30 min were measured at a wavelength of 517 nm. The same experimental method was applied to the control sample by adding methanol instead of it. The % inhibition values of the samples were determined using the equation below. In addition, IC_{50} values were calculated.

$$\%\boldsymbol{inhibitionofradicals}(\boldsymbol{DPPH}\cdot) = \frac{(\boldsymbol{ControlAbs} - \boldsymbol{Sample/StandartAbs})}{\boldsymbol{ControlAbs}}\boldsymbol{x}100 \quad (2)$$

2.2.3. Determination of antidiabetic activity

2.2.3.1. α-Glucosidase enzyme inhibition. α-Glucosidase enzyme activity was investigated in the presence and absence of ligand, complex, and standard drug acarbose [47]. The α-glucosidase enzyme (0.2 U) to be used in the study was prepared in 0.1 M phosphate buffer (pH = 6.8). 5 mM p-NPG (p-Nitrophenyl-α-D-glucopyranoside) solution was used as the substrate. To determine the enzyme activity, 20 μL of enzyme solution and 100 μL of p-NPG were mixed. It was kept at 37 °C for 20 min. After adding 80 μL of 0.1 M Na_2CO_3 to the medium, the absorbance of the sample was measured at the 405 nm wavelength. To determine the inhibitory effects of ligand, complex, and standard substances on the α-glucosidase enzyme, solutions were prepared at concentrations of 25, 50, and 100 μg/mL. 50 μL of these prepared solutions were taken and mixed with 20 μL of enzyme solution. All samples were kept at 37 °C for 10 min. 100 μL of substrate was added to the samples and kept at 37 °C for 15 min. Then, 80 μL of Na_2CO_3 solution was added, and the absorbance values of the samples were recorded at a 405 nm wavelength. The α-glucosidase enzyme inhibition percentage values of the samples in this study were determined by the following formula.

$$\boldsymbol{\alpha - glucosidaseinhibition}(\%) = \frac{(\boldsymbol{GlucosidaseAbs} - \boldsymbol{Sample/AcarboseAbs}}{\boldsymbol{GlucosidaseAbs}}\boldsymbol{x}100 \quad (3)$$

Glucosidase Abs: Absorbance of the tube considered as 100 % active

Sample/Acarbose Abs: Absorbance values of samples − sample blank absorbance values.

2.2.3.2. α-Amylase enzyme inhibition. The α-amylase activities of ligand, complex, and standard acarbose substances were determined in the presence and absence of these samples [48]. A solution of the α-amylase enzyme (1.5 U) was made using 20 mM phosphate buffer (pH = 6.8). Starch solution (1 %) was used as the substrate. To determine the activity of the α-amylase enzyme, 0.5 mL of enzyme solution and 0.5 mL of starch solution were mixed and kept at 25 °C for 15 min. 1 mL of DNS (3,5-dinitrosalicylic acid) solution was added to the sample and boiled for 5 min. After the sample was cooled, 7.5 mL of pure water was added. A control tube was prepared by replacing the enzyme with 0.5 mL of buffer. The absorbance values of the samples were determined at a wavelength of 540 nm. In order to investigate the inhibitory effect of ligand, complex, and standard acarbose substances on the α-amylase enzyme, samples of these substances were prepared at concentrations of 25, 50, and 100 μg/mL. 0.5 mL of sample was taken and combined with 0.5 mL of enzyme solution. It was kept at 37 °C for 15 min. 0.5 mL of starch and 1 mL of DNS solution were added to the medium, and the samples were boiled. 7.5 mL of pure water was added to the cooled samples, and their absorbance was measured at the 540 nm wavelength. Blank samples of all samples were prepared at the same time. The following formula was used to calculate the enzyme inhibition percentages of ligand, complex, and standard (acarbose) samples.

$$\boldsymbol{\alpha - amylaseinhibition}(\%) = \frac{(\boldsymbol{AmylaseAbs} - \boldsymbol{Sample/AcarboseAbs}}{\boldsymbol{AmylaseAbs}}\boldsymbol{x}100 \quad (4)$$

Amylase Abs: Absorbance of the tube considered as 100 % active

Sample/Acarbose Abs: Absorbance values of samples − sample blank absorbance values.

2.2.4. Statistical analysis

Biological activity studies in the study were conducted on three samples. The mean and standard deviations of the results were determined. Additionally, inhibitory concentration (IC_{50}) values of all samples were calculated.

2.2.5. X-ray crystallography

X-ray diffraction data were collected on a Bruker D8 QUEST diffractometer at 296(2) K using graphite-monochromated Mo Kα radiation by applying the φ and ω scan methods. Data collection was carried out using APEX2 [49], while cell refinement and data reduction

Table 1
Crystal data and structure refinement parameters for $[Ag(EIMC)_2]ClO_4$ complex.

CCDC depository	2,428,121
Color/shape	Colorless/block
Chemical formula	$[Ag(C_6H_8N_2O_2)_2]^+ \cdot ClO_4^-$
Formula weight	487.61
Temperature (K)	296(2)
Wavelength (Å)	0.71073 Mo Kα
Crystal system	Triclinic
Space group	$P-1$ (No. 2)
Unit cell parameters	
a, b, c (Å)	7.0981(11), 9.6636(16), 14.487(3)
α, β, γ (°)	103.201(7), 94.174(7), 106.251(4)
Volume (Å^3)	918.8(3)
Z	2
$D_{calc.}$ (g/cm^3)	1.762
μ (mm^{-1})	1.290
Absorption correction	Multi-scan
$T_{min.}$, $T_{max.}$	0.5720, 0.7454
F_{000}	488
Crystal size (mm^3)	0.11 × 0.07 × 0.06
Diffractometer	Bruker D8 QUEST
Measurement method	φ and ω scan
Index ranges	$-8 \le h \le 8$, $-12 \le k \le 12$, $-18 \le l \le 18$
θ range for data collection (°)	$2.920 \le \theta \le 26.547$
Reflections collected	15,737
Independent/observed reflections	3764/2017
Refinement method	Full-matrix least-squares on F^2
Data/restraints/parameters	3764/114/277
Goodness-of-fit on F^2	1.031
Final R indices [$I > 2\sigma(I)$]	$R_1 = 0.0790$, $wR_2 = 0.1759$
R indices (all data)	$R_1 = 0.1601$, $wR_2 = 0.2096$
$\Delta\rho_{max.}$, $\Delta\rho_{min.}$ (e/Å^3)	1.47, −0.96

were applied using SAINT [49]. The structure was solved by a dual-space algorithm using SHELXT-2018 [50] and refined by means of the full-matrix least-squares calculations on F^2 using SHELXL-2019 [51]. Oxygen atoms of the perchlorate anion show positional disorder, and the refined site-occupancy factors of the disordered atoms are 0.612(7)% for the major position and 0.388(7)% for the minor position. All H atoms were located in difference maps and then treated as riding atoms, fixing the bond lengths at 0.93, 0.97, and 0.96 Å for CH, CH_2, and CH_3 atoms, respectively. The displacement parameters of the H atoms were included as $U_{iso}(H) = 1.2U_{eq}$ ($1.5U_{eq}$ for CH_3). Crystal data, data collection, and structure refinement details are collected in Table 1. Molecular graphics were created by using OLEX2 [52].

3. Results and discussion

3.1. Description of the structure

The solid-state structure of $[Ag(EIMC)_2]ClO_4$ has been unambiguously determined by single-crystal X-ray diffraction analysis and shown in Fig. 1.

The structure of the monomeric $[Ag(1\text{-}Carbim)_2]ClO_4$ complex crystallizes as a salt in the triclinic space group $P-1$ with Z = 2. The asymmetric unit of $[Ag(EIMC)_2]ClO_4$ comprised two half-occupied Ag(I) cations residing on an inversion center, two 1-carbethoxyimidazole (1-Carbim) ligands, and one ClO_4^- counter-anion. The Ag(I) is coordinated with two 1-Carbim ligand units via the imidazole N-atom, where the two ligand units are in the anti configuration to one another. Due to symmetry considerations the two Ag—N bonds are equidistant [2.148(6) Å for Ag1—N1 and 2.118(6) Å for Ag2—N3, and N—Ag—N angles are 180°]. Each of the Ag(I) ions also weakly interacts with the perchlorate anion through Ag—O interactions with Ag1—O5 = 2.7829(4) Å and Ag2—O8 = 2.8160(4) Å, which fall within the sum of the van der Waals radii of Ag = 1.72 and O = 1.52 Å [53], which is 3.24 Å. The Ag···Ag distance of 3.5491(6) Å is significantly close to the van der Waals radii sum of two Ag atoms (3.44 Å) [53], which indicates a weak argentophillic interaction between the two Ag(I) ions.

3.2. Optimized geometric structure

In this part of the study, by optimizing the initial geometry obtained from the XRD analysis of the synthesized complex structure, theoretical values corresponding to the experimental bond length and bond angles were calculated and compared with each other. Experimental bond lengths and bond angles obtained from XRD data and calculated values for both the free ligand and the synthesized complex are given in Table 2, while the geometries of the optimized structures are presented in Fig. 1.

The Ag1—N1 and Ag1—$N1^i$ bond lengths were found to be 2.148 Å in XRD analysis. In theoretical calculations, these bond lengths were calculated as 2.295 Å. In the imidazole ring of the [Ag(EIMC)2]ClO4 complex, the N1—C1 and N1—C2 bond lengths were found to be 1.293 and 1.395 Å experimentally, while they were calculated as 1.312 and 1.388 Å theoretically. These bond lengths of the free ligand were found to be 1.301 and 1.388 Å in the calculations.

The N2—C1 and N2—C3 bond lengths were found to be 1.370 and 1.415 Å, according to XRD data. Theoretical calculations determined these bond lengths to be 1.371 and 1.394 Å for the complex and 1.386 and 1.395 Å for the free ligand. In addition, the C2—C3 bond length in the imidazole ring was determined as 1.340 Å in the XRD data of the $[Ag(EIMC)_2]ClO_4$ complex. This bond length was calculated as 1.358 Å for the complex and 1.361 Å for the EIMC ligand.

The N2—C4 bond length connecting the imidazole ring to the carboxylate group was found experimentally to be 1.415 Å. It was theoretically calculated as 1.419 and 1.405 Å for the complex and free ligand.

The O1—C4, O2—C4, and O2—C5 bond lengths were determined as 1.197, 1.315, and 1.454 Å by XRD analysis. The theoretical values of these bond lengths for the $Ag(EIMC)_2]ClO_4$ complex were calculated as 1.198, 1.332, and 1.460 Å, respectively, while for the EIMC ligand they were calculated as 1.204, 1.336, and 1.457 Å. The experimental and calculated values of the C5—C6 bond of the ethyl group in the complex are 1.419 and 1.512 Å. This value for the free ligand was theoretically obtained as 1.513 Å.

The C1—N1—C2, C1—N2—C3, N1—C1—N2, C3—C2—N1, and C2—C3—N2 bond angles of the imidazole ring of the synthesized complex were experimentally found to be 106.8, 108.6, 109.8, 109.3, and 105.4°, respectively. The theoretical values of these bond angles were calculated as 106.8, 107.5, 110.3, 109.9, and 105.4°, respectively. These angle values for the free ligand were found to be 105.7, 106.4, 111.6, 110.9, and 105.2 in theoretical calculations.

The C1—N1—Ag1 and C2—N1—Ag1 bond angles were found to be 127.5 and 125.6° in experimental analysis and 119.9 and 133.2° in theoretical calculations. The N1—Ag1—$N1^i$ angle is 180.0° experimentally and 156.8° theoretically.

Although no significant differences were observed in the values of the experimental and theoretical bond angles of the imidazole ring, there are deviations in these bond angles. The reason for these deviations is that the theoretical calculations were made for an isolated structure that is not exposed to any coulombic interaction in the gas phase. However, the isolated structure in the crystal lattice is exposed to coulombic interaction with neighboring structures.

Finally, we calculated root mean square deviation (RMSD) values in this section to demonstrate the agreement between experimental and theoretical bond lengths and bond angles. For the bond length, the calculated RMSD values for both the free ligand and the synthesized complex were obtained as 0.03 and 0.67. According to these results, it can be said that the calculated bond lengths are in excellent agreement with the experimental values. The calculated RMSD values for the bond angles are 1.51 for the EIMC ligand and 5.87 for the $[Ag(EIMC)_2]ClO_4$ complex. These values are also at acceptable levels. [54,55].

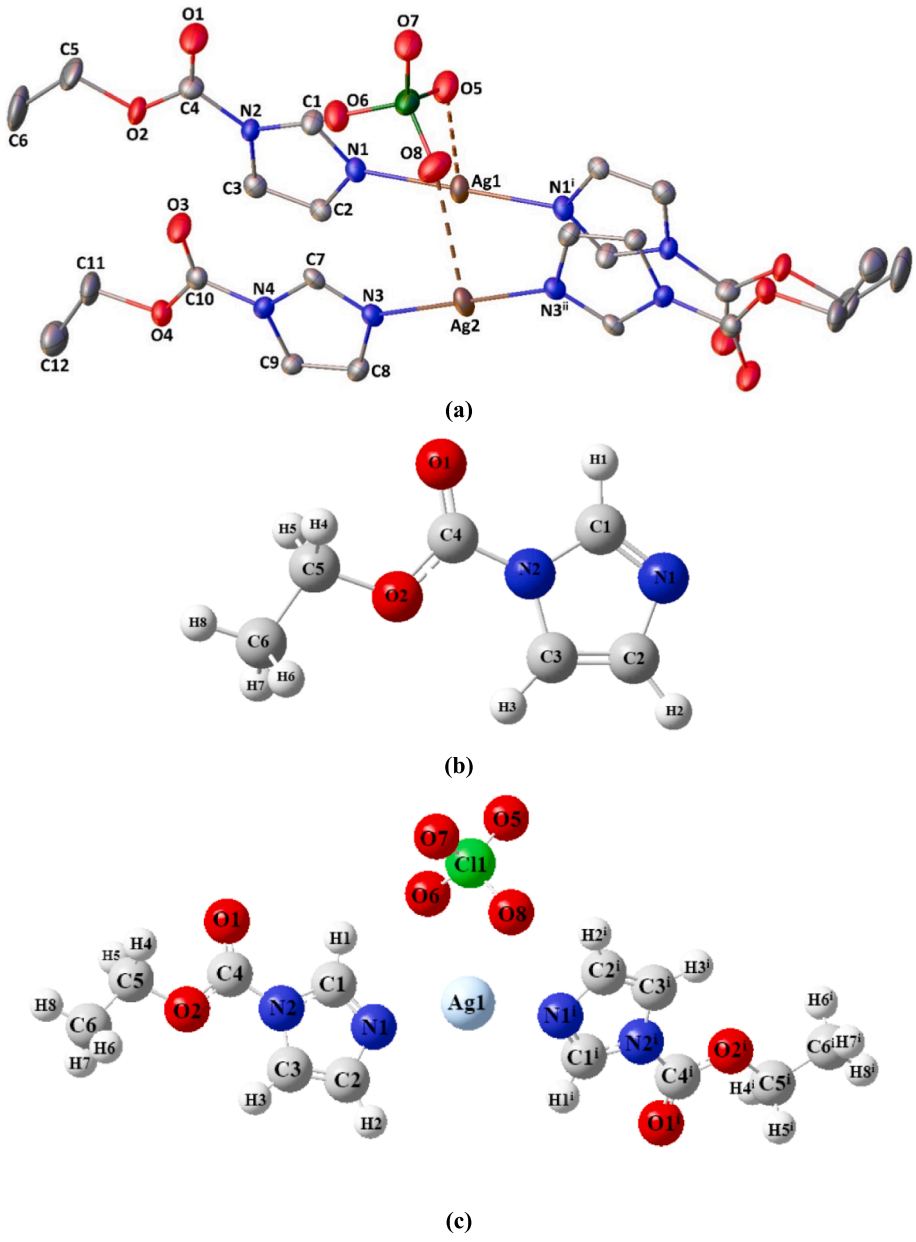

Fig. 1. Molecular structure of $[Ag(EIMC)_2]ClO_4$ showing atom-numbering scheme. Displacement ellipsoids are drawn at the 20 % probability level and H atoms have been omitted for clarity. Only major part of the disordered oxygen atoms of the perchlorate anion is shown [Symmetry codes: $^{i} -x+1, -y+1, -z$; $^{ii} -x+2, -y+1, -z$] (**a**) and, optimized geometric structure of the EIMC ligand (**b**) and the $[Ag(EIMC)_2]ClO_4$ complex (**c**).

3.3. Frequency analysis

The FT-IR spectra of the EIMC molecule and $[Ag(EIMC)_2]ClO_4$ complex were recorded, and the theoretical wavenumbers corresponding to the experimental values were calculated. The scale factor was used to ensure the best fit between experimental and theoretical values. A scale factor of 0.983 was used for wavelengths below 1800 cm^{-1} [56], and a scale factor of 0.955 was used for wavelengths above 1800 cm^{-1} [36]. In addition, the vibration modes corresponding to the wavenumbers were calculated and assigned according to their total energy distribution (TED) (≥10 %) using the VEDA program [57]. The experimental IR spectra are presented in Fig. 2, and the selected wavenumbers are listed in Table 3 and Table 4 with their mode assignments.

3.3.1. C–H vibrations

The region between 3100 and 3000 cm^{-1} is primarily where we observe the C–H stretching vibrations of molecules. While the C–H stretching vibration of the imidazole ring of the free ligand was recorded at 3137 (asym, vw), this stretching vibration was assigned at 3138 (asym, vw) cm^{-1} for the synthesized complex. In the calculations, the theoretical value corresponding to the experimental value of the EIMC ligand was found at 3120 cm^{-1}. The theoretical value for the complex was calculated as 3130 cm^{-1}. It has been reported in the literature that the C–H stretching vibration of the imidazole ring of the 4-(4-chlorophenyl)-1H-imidazole molecule was observed at 3113 cm^{-1} and calculated at 3164 cm^{-1} [58]. In another study, the C–H stretching vibrations for the imidazole ring of the 2-ethylimidazole molecule are assigned at 3134 cm^{-1} in the FT-IR spectrum and 3141 cm^{-1} in the FT-Ra spectrum [59].

Asymmetric C–H stretching vibrations were observed for the ethyl group of the EIMC ligand at 2990 (vw) and 2947 (vw) cm^{-1}. For this group, the theoretical asymmetric stretching vibrations were calculated at 2982 and 2968 cm^{-1}. Also this vibration was observed at 2296 (cw) and calculated 3108 cm^{-1} for the synthesized $[Ag(EIMC)_2]ClO_4$

Table 2
Calculated bond lengths and bond angles of the EIMC ligand and $[Ag(EIMC)_2]ClO_4$ complex, as well as the XRD data of the $[Ag(EIMC)_2]ClO_4$ complex.

Parameters	Bond Lengths (Å)			Parameters	Bond angles (°)		
	EIMC	$[Ag(EIMC)_2]ClO_4$			EIMC	$[Ag(EIMC)_2]ClO_4$	
	Calculated	Calculated	XRD[a]		Calculated	Calculated	XRD
Ag1—N1	–	2.295	2.148 (6)	C1—N1—C2	105.7	106.8	106.8 (6)
Ag1—N1^{i}	–	2.295	2.148 (6)	N1—Ag1—N1^{i}	–	156.8	180.0
N1—C1	1.301	1.312	1.293 (10)	C1—N1—Ag1	–	119.9	127.5 (5)
N1—C2	1.388	1.388	1.395 (9)	C2—N1—Ag1	–	133.2	125.6 (6)
N2—C1	1.386	1.371	1.352 (9)	C1—N2—C3	106.4	107.5	108.6 (7)
N2—C3	1.395	1.394	1.370 (10)	C1—N2—C4	124.4	123.9	123.8 (7)
N2—C4	1.405	1.419	1.415 (11)	C3—N2—C4	129.1	128.6	127.6 (7)
C2—C3	1.361	1.358	1.340 (12)	N1—C1—N2	111.6	110.3	109.8 (7)
O1—C4	1.204	1.198	1.197 (9)	C3—C2—N1	110.9	109.9	109.3 (7)
O2—C4	1.336	1.332	1.315 (10)	C2—C3—N2	105.2	105.4	105.4 (7)
O2—C5	1.457	1.460	1.454 (11)	O1—C4—O2	126.2	127.1	127.9 (9)
C5—C6	1.513	1.512	1.419 (14)	O1—C4—N2	123.2	122.9	121.8 (8)
Cl1—O5A	–	1.478	1.511 (9)	O2—C4—N2	110.5	109.9	110.3 (7)
Cl1—O6A	–	1.523	1.437 (9)	C6—C5—O2	107.4	107.4	109.8 (8)
Cl1—O7A	–	1.478	1.405 (8)	C4—O2—C5	115.9	115.7	117.5 (7)
Cl1—O8A	–	1.524	1.455 (10)	O6A—Cl1—O5A	–	110.0	105.1 (8)
RMSD	**0.03**	**0.67**	–	O7A—Cl1—O5A	–	111.7	112.8 (10)
–	–	–	–	O8A—Cl1—O5A	–	109.5	108.0 (8)
–	–	–	–	O7A—Cl1—O6A	–	109.6	109.2 (7)
–	–	–	–	O8A—Cl1—O6A	–	105.8	106.5 (8)
–	–	–	–	O7A—Cl1—O8A	–	109.4	114.7 (8)
–	–	–	–	**RMSD**	**1.51**	**5.87**	–

Å: Angstrom; °: degree.

complex. In the literature, the symmetric and asymmetric C–H stretching vibrations for the ethyl group of 2-ethylimidazole molecule were reported at 3110 and 3045 3022, 2980 and 2889 cm^{-1} in the FT-IR spectrum [59].

3.3.2. C–C vibrations

In the IR spectrum, the C=C stretching vibrations for the organic heterocyclic molecule rings are expected to be observed in the range of 1650–1400 cm^{-1} [59]. For the imidazole ring of the EIMC molecule, C=C stretching vibrations were observed at 1529 (vw), 1476 (m), and 1385 (vs) cm^{-1}, and the calculated values corresponding to these

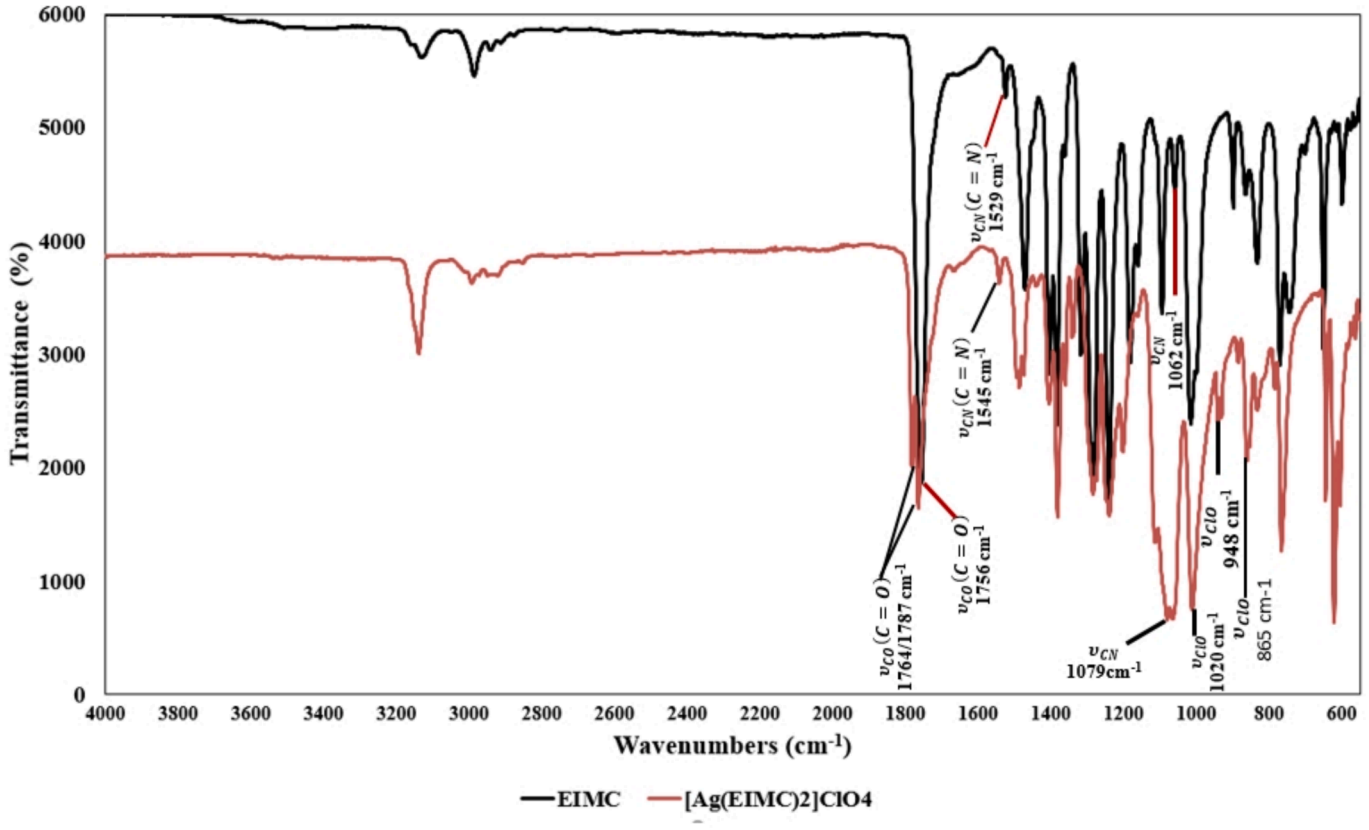

Fig. 2. Experimental FT-IR spectra of the EIMC ligand and $[Ag(EIMC)_2]ClO_4$ complex.

Table 3
Recorded and calculated frequency values with the total energy densities of the EIMC ligand.

Calculated				Observed	
Mode	Fre	Fre[a]	I^{b}_{IR}	IR	TED
11	604	594	0.72	595 *m*	$84\Gamma_{CCCN}$
12	661	650	4.45	654 s	$76\Gamma_{CCNC} + 13\Gamma_{HCNC}$
13	747	735	6.55	742 *m*	$74\Gamma_{HCCN} + 10\Gamma_{HCNC}$
14	779	766	9.24	775 s	$73\Gamma_{HCCO}$
17	842	828	5.61	835 *m*	$73\Gamma_{HCNC} + 16\Gamma_{CCNC}$
19	884	869	0.20	868 w	$15\Gamma_{HCCN} + 66\Gamma_{HCNC}$
20	910	895	0.71	902 *m*	$83\delta_{CCN}$
22	1034	1016	42.34	1018 vs	$59\upsilon_{CC} + 10\delta_{CNC}$
23	1083	1065	0.73	1062 w	$20\upsilon_{CN} + 42\delta_{CCH}$
24	1122	1103	5.66	1096 *m*	$37\upsilon_{CN} + 12\delta_{CCH} + 31\delta_{HCN}$
26	1177	1157	0.95	1162 w	$18\delta_{CCH} + 57\Gamma_{HCOC}$
27	1197	1177	44.05	1182 s	$35\upsilon_{CO} + 12\upsilon_{CN} + 11\delta_{HCN}$
28	1263	1241	62.24	1242 vs	$66\delta_{NCH}$
29	1297	1275	41.51	1279 vs	$12\upsilon_{CN} + 12\delta_{HCN} + 14\delta_{CNC} + 13\delta_{COC}$
31	1323	1301	78.87	1319 s	$34\upsilon_{CN} + 12\delta_{HCN}$
33	1417	1393	36.17	1385 vs	$12\upsilon_{CC} + 12\upsilon_{CN} + 40\delta_{HCH}$
34	1436	1412	23.93	1413 s	$12\upsilon_{CN} + 32\Gamma_{HCOC}$
37	1505	1480	20.43	1476 *m*	$50\upsilon_{CC} + 15\delta_{CCH} + 12\delta_{HCN}$
39	1565	1538	1.02	1529 vw	$45\upsilon_{CN}(C=N) + 26\upsilon_{CC}(C=C) + 16\delta_{HCN}$
40	1804	1773	100	1756 vs	$86\upsilon_{CO}$(C=O)
44	3107	2968	5.51	2947 vw	$97\upsilon_{CH}$(asym/ethyl group)
45	3123	2982	8.26	2990 vw	$99\upsilon_{CH}$(asym/ethyl group)
47	3267	3120	0.89	3137 vw	$99\upsilon_{CH}$(asym/imidazole ring)

υ: stretching, *δ*: in-plane bending,γ: out-of bending Γ: torsion, s: strong, m: medium, w: weak, v: very.
[a]Scaled wavenumbers calculated at B3LYP/6–311++G(d,p) using scaling factors 0.983 for the wavenumber less than 1800 cm^{-1} [56] and 0.955 above 1800 cm^{-1} [36].
[b]Relative absorption intensities normalized with highest peak absorption equal to 100.
[c]Total energy distribution level (TED) less than 10% are not shown.

Table 4
Recorded and calculated frequency values with the total energy densities of the $[Ag(EIMC)_2]ClO_4$ complex.

Calculated				Observed	
Mode	Fre	Fre[a]	I^{b}_{IR}	IR	TED
40	557	548	4.27	555 w	$12\Gamma_{CHOCl} + 28\Gamma_{OClOH}$
42	15	605	0.26	619 vs	$15\Gamma_{CNCH} + 10\Gamma_{CNCC} + 1\Gamma_{NCHO} + 17\Gamma_{CNCO}$
43/44	662	651	2.87	646 s	$11\Gamma_{NAgNC} + 14\Gamma_{CNCH}$
47/48	779	765	2.58	769 vs	$12\Gamma_{CNCH} + 10\Gamma_{OCOC} + 22\Gamma_{CNCO}$
54	849	834	2.39	833 *m*	$16\Gamma_{AgNCH} + 40\Gamma_{CNCH}$
58	882	867	44.86	865 *m*	$15\upsilon_{ClO} + 10\delta_{OClO}$
63	989	972	59.08	948 *m*	$28\upsilon_{ClO} + 10\delta_{OClO}$
68	1050	1032	38.24	1020 vs	$26\upsilon_{ClO} + 13\delta_{OClO}$
69	1088	1070	2.17	1066 vs	$10\upsilon_{CN} + 21\delta_{NCH} + 14\delta_{CCH}$
70	1091	1073	3.76	1079 vs	$10\upsilon_{CN} + 16\delta_{NCH} + 12\delta_{CCH}$
74	1135	1115	1.76	1120 s	$14\delta_{CCH} + 17\Gamma_{HCCH}$
77/78	1209	1188	40.02	1198 s	$13\upsilon_{CN} + 10\upsilon_{CO} + 16\delta_{NCH}$
79/80	1262/1266	1241/1244	21.89	1244 s	$23\delta_{HCH}$
81/82	1296/1298	1274/1276	100.00	1285 s	$27\delta_{NCH}$
89	1413	1389	25.98	1385 s	$10\upsilon_{CN} + 10\upsilon_{CC} + 18\delta_{HCH}$
91/92	1434	1410	8.12	1408 *m*	$10\delta_{HCH} + 10\delta_{NCN} + 10\Gamma_{HCCH}$
97/98	1509/1515	1484/1489	19.27	1490 *m*	$15\upsilon_{CN} + 10\upsilon_{CC} + 29\delta_{NCH} + 10\delta_{CCH}$
101/102	1569/1579	1543/1552	0.99	1545 vw	$12\upsilon_{CN} + 10\upsilon_{CC} + 18\delta_{NCH} + 10\delta_{CCH}$
103/104	1812/1829	1781/1798	50.89	1764/1787 s	$21\upsilon_{CO} + 10\delta_{CNC} + 10\delta_{NCO}$
115/116	3255	3108	9.03	2996 vw	$40\upsilon_{CH}$(asym/ethyl group)
118	3278	3130	1.25	3138 w	$75\upsilon_{CH}$(asym/imidazole ring)

υ: stretching, *δ*: in-plane bending,γ: out-of bending Γ: torsion, s: strong, m: medium, w: weak, v: very.
[a]Scaled wavenumbers calculated at B3LYP/6–311++G(d,p) using scaling factors 0.983 for the wavenumber less than 1800 cm^{-1} [56] and 0.955 above 1800 cm^{-1} [36].
[b]Relative absorption intensities normalized with highest peak absorption equal to 100.
[c]Total energy distribution level (TED) less than 10% are not shown.

experimental values were found at 1538, 1480, and 1393 cm^{-1}. Also, these vibration values for the synthesized $[Ag(EIMC)_2]ClO_4$ were observed at 1545 (vw), 1490 (m), and 1385 (s) cm^{-1} in the IR spectrum and calculated at 1543/1552, 1484/1489, and 1389 cm^{-1}. In the imidazole ring of the 4-(4-fluoro-phenyl)-1H-imidazole molecule, C=C stretching vibrations were reported at 1513 and 1293 cm^{-1} in the FT-Ra spectrum [58]. In another study, the C=C stretching vibrations for the imidazole ring of the 4-(4-chlorophenyl)-1H-imidazole molecule were found to be 1505 and 1400 cm^{-1} in the IR spectrum and 1515 and 1403 cm^{-1} in the Ra spectrum. Theoretical values are calculated as 1528 and 1401 cm^{-1} [60].

3.3.3. C=N and C-N vibrations

The C=N stretching vibrations are observed in the region of 1672–1566 cm^{-1} [61,62]. This vibration value for the EIMC molecule was observed at 1529 (vw) cm^{-1} and calculated at 1538 cm^{-1}. This vibration value for the synthesized complex was recorded at 1545 (vw) cm^{-1} with a shift of approximately 16 cm^{-1}. This shift in the C=N stretching vibration is an indication that the Ag atom is coordinated with the N atom in the imidazole ring of the EIMC ligand. The C-N stretching vibration is usually seen between 1400 and 1200 cm^{-1}. These stretching vibrations for the EIMC molecule were observed at 1413 (s), 1385 (vs), 1319 (s), and 1279 (vs) cm^{-1} in the FT-IR spectrum and were calculated at 1412, 1393, 1301, and 1275 cm^{-1}. For the $[Ag(EIMC)_2]ClO_4$, these vibration values occurred at 1408 (m), 1385 (s), and 1198 (s) cm^{-1} in the FT-IR spectrum and were calculated at 1410, 1398, and 1188 cm^{-1}. The C=N and C-N stretching vibrations for the imidazole ring of the 2-ethyl-1H-benzo[d]imidazole molecule also appeared in the FT-Ir spectrum at 1541 and 1407 cm-1, respectively [63].

3.3.4. C=O and C-O vibrations

The C=O stretching vibrations are generally expected to be observed in the region between 1700 and 1800 cm^{-1} [64]. In the recorded FTIR spectrum of the EIMC molecule, the C=O stretching vibration was observed at 1756 (s) cm^{-1}, and the frequency value for this stretching vibration was calculated at 1773 cm^{-1}. In the FT-IR spectrum of the synthesized complex, C=O stretching vibrations were observed at 1764 and 1787 cm^{-1} (due to the presence of two ligands in the structure) and were calculated at 1781 and 1789 cm^{-1}. In the literature, this vibration band for the ethyl-6-chloronicotinate molecule was observed at 1724 cm^{-1} in the IR spectrum. In theoretical calculations, the unscaled value was reported as 1766 cm^{-1}, while the scaled value was reported as 1692 cm^{-1} [65].

The C-O stretching vibration was observed at 1182 (s) cm^{-1} and calculated at 1177 cm^{-1}, while this stretching vibration for the complex was recorded at 1198 (s) and calculated at 1188 cm^{-1}. For the ethyl-6-chloronicotinate molecule, the C-O stretching vibration was reported at 1125 and 854 cm in the IR spectrum [65].

3.3.5. Cl-O vibrations

The peaks observed at 1020 (vs), 948 (m), and 865 cm^{-1} in the FT-IR

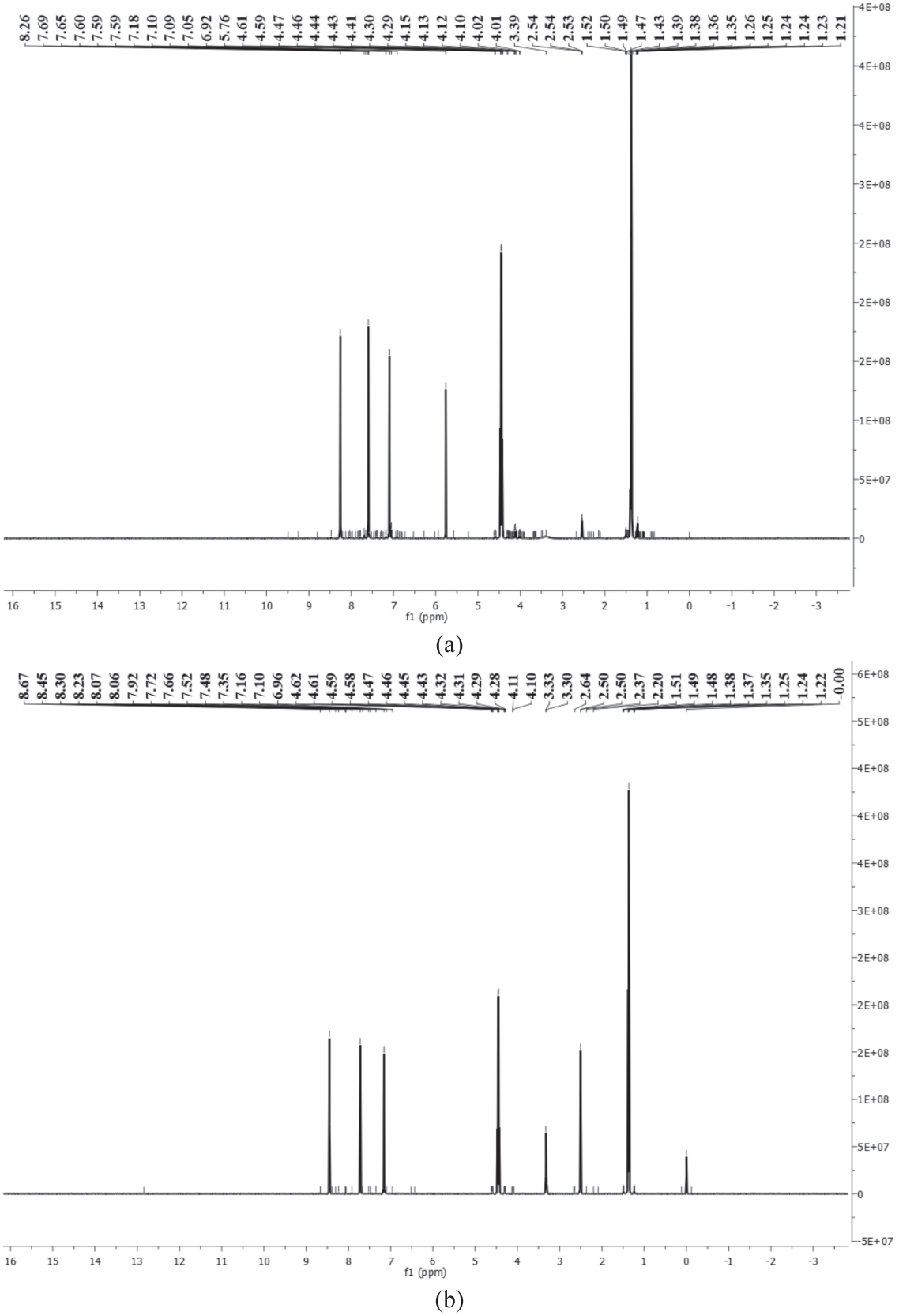

Fig. 3. Experimental ^{1}H and ^{13}C NMR spectra of the EIMC ligand and the $[Ag(EIMC)_2]ClO_4$ complex. a) ^{1}H NMR spectrum of the EIMC ligand b) ^{1}H NMR spectrum of the $[Ag(EIMC)_2]ClO_4$ complex. c) ^{13}C NMR spectrum of the EIMC ligand. d) ^{13}C NMR spectrum of the$[Ag(EIMC)_2]ClO_4$ complex.

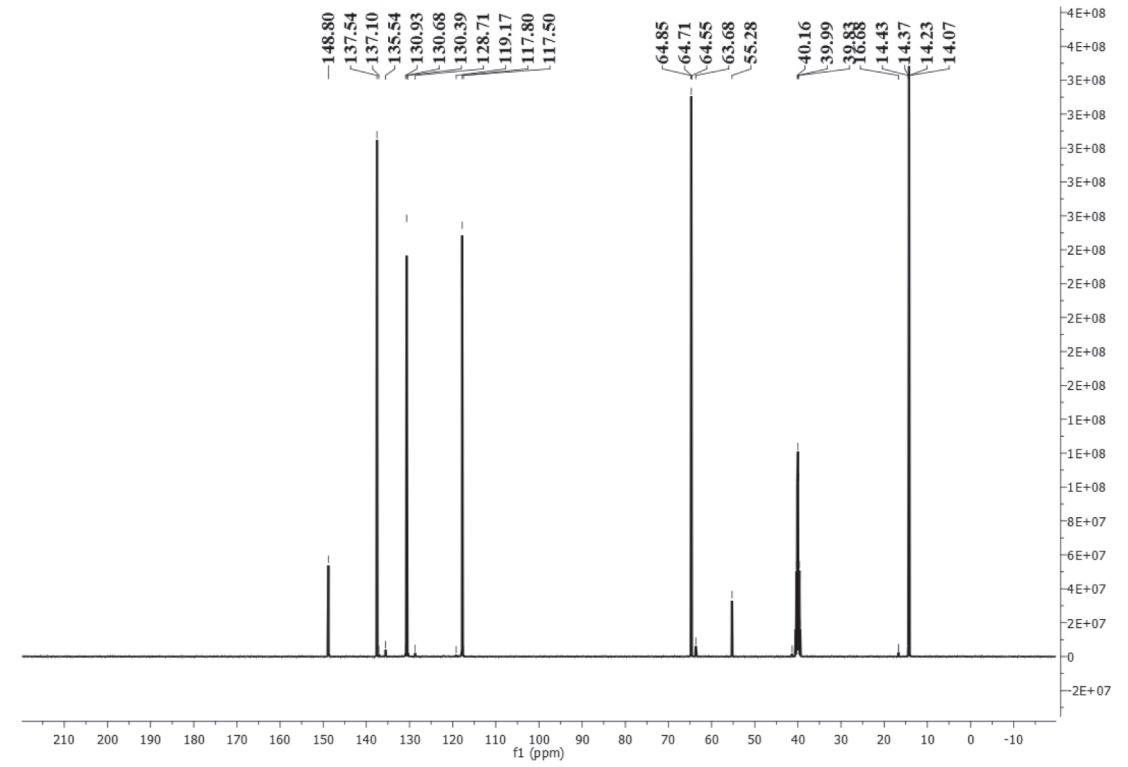

(c)

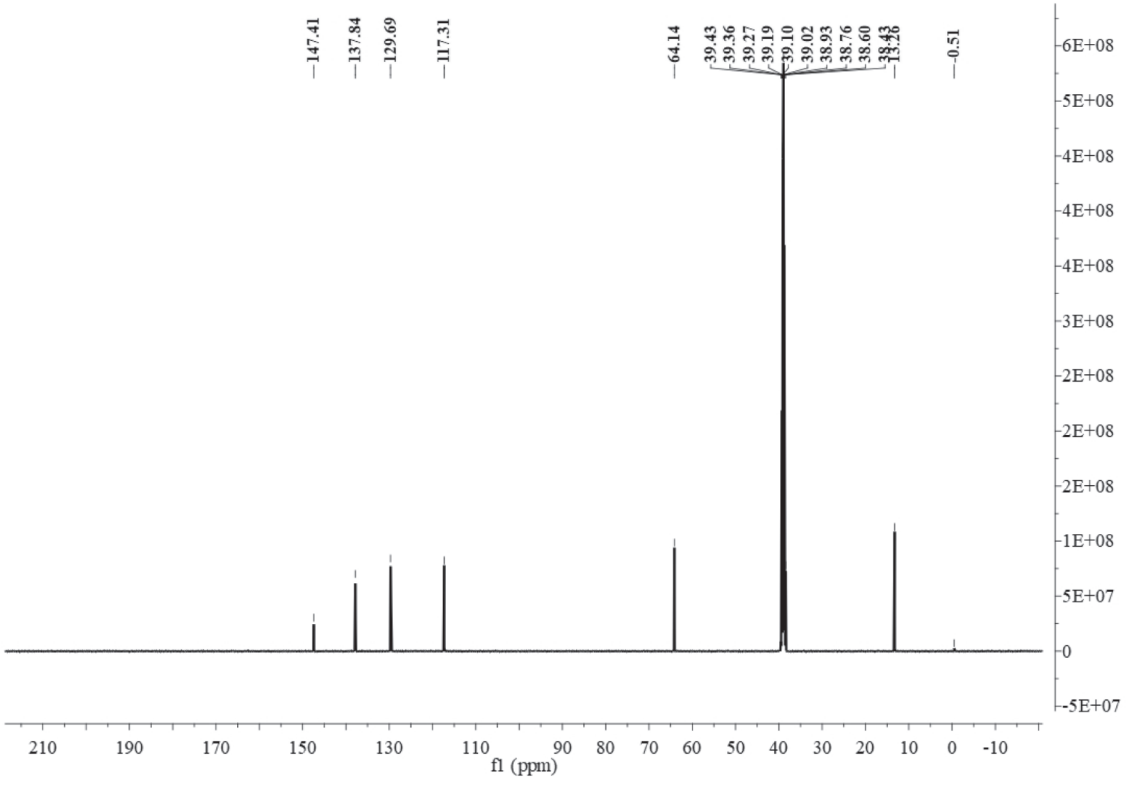

(d)

Fig. 3. (*continued*).

spectrum of the $[Ag(EIMC)_2]ClO_4$ complex belong to the Cl-O stretching vibration. In the calculations, theoretical vibration values were obtained at 1032, 972, and 867 cm^{-1}, corresponding to these experimental values. The presence of these peaks, which are not observed in the spectrum of the free ligand, is spectroscopic evidence that complexation has occurred. A study in the literature synthesized an N-(pyridin-2-yl)

Table 5
^{1}H and ^{13}C NMR chemical shift values of the EIMC ligand and $[Ag(EIMC)_2]ClO_4$ complex.

	EIMC			$[Ag(EIMC)_2]ClO_4$	
Atoms	Experimetal	6–311 + G (2d,p)	Atoms	Experimetal	6–311 + G (2d,p)
H_1	8.26	8.32	H1/ $H1^i$	8.45	9.18/8.54
H_2	7.09	7.23	H2/ $H2^i$	7.15	8.02/7.30
H_3	7.59	7.67	H3/ $H3^i$	7.72	7.78/7.70
H_4	4.42	4.42	H4/ $H4^i$	4.43	4.47/4.49
H_5	4.42	4.42	H5/ $H5^i$	4.43	4.47/4.49
H_6	1.39	1.48	H6/ $H6^i$	1.36	1.51
H_7	1.39	1.48	H7/ $H7^i$	1.36	1.51
H_8	1.36	1.33	H8/ $H8^i$	1.36	1.36
C1	137.54	143.15	$C1/C1^i$	137.84	146.94/ 144.12
C2	130.67	136.27	$C2/C2^i$	129.85	136.33/ 138.13
C3	117.80	122.69	$C3/C3^i$	117.31	123.39/ 122.64
C4	148.79	156.44	$C4/C4^i$	147.52	155.41/ 155.87
C5	64.71	69.05	$C5/C5^i$	64.22	69.94/70.09
C6	14.22	13.97	$C6/C6^i$	13.26	13.96

pyridin-2-amine molecule from a C10H9N3 AgClO4 complex. In this study, IR spectra of both the synthesized complex and $AgClO_4$ were recorded. Cl-O stretching vibrations were recorded at 1095, 1000, 884, and 725 cm^{-1} in the spectrum of $AgCLO_4$. While these vibration values were recorded at 1094, 1048, 928, and 779 cm^{-1} for the synthesized complex, they were calculated at 1085, 1014, 928, and 779 cm^{-1} [66].

Finally, in this part of our study, a correlation graph was drawn to show the harmony between the wavenumbers in the recorded FT-IR spectrum of the EIMC molecule and the $[Ag(EIMC)_2]ClO_4$ complex and the calculated values (see Supplementary Fig. S1). The equation of this graph was determined, and the R^2 value belonging to its slope was calculated. The R^2 values obtained for the graph slopes are 0.9998 for the EIMC ligand and 0.9990 for the $Ag(EIMC)_2ClO_4$ complex. According to this result, we can say that there is an excellent agreement between the experimental and calculated wavenumbers.

3.4. ^{1}H and ^{13}C NMR analyses

Chemical shift analysis is an important method employed in the structural investigation of organic and inorganic compounds. The ^{1}H NMR spectrum reveals the number of different proton types and their immediate surroundings. Additionally, the ^{13}C NMR spectrum provides helpful information regarding the structural characteristics of individual carbon atoms inside the compounds. Recently, NMR spectroscopy and computer modeling techniques have been used together to comprehensively understand and explain the structure of complex compounds. [67]. Experimental spectra of the EIMC ligand and $[Ag(EIMC)_2]ClO_4$ complex were recorded in DMSO, and theoretical calculations were performed in the same solvent. While the recorded spectra were presented in Fig. 3, the experimental and theoretical chemical shift values are listed in Table 5.

The experimental shift values for H4 and H5 atoms of the EIMC ligand were recorded and calculated at 4.42 ppm. The chemical shift values of H4/H4i and H5/H5i atoms of the [Ag(EIMC)2]ClO4 complex were recorded at 4.43 ppm and calculated at 4.47/4.49 ppm. While the experimental value for the H3 atom of the free ligand was observed at

Table 6
Energy values of the EIMC ligand and the $[Ag(EIMC)_2]ClO_4$ complex.

Molecular Orbitals	Energy (eV)			Energy gap (eV)		Ionization potential (I) (eV)		Electron affinity (A) (eV)		Global hardness (η) (eV)		Electronegativity (χ) (eV)		Chemical potential (μ_c) (eV)		Global softness (σ) $(eV)^{-1}$		Global electrophilicity (ω) (eV)	
	*	**		*	**	*	**	*	**	*	**	*	**	*	**	*	**	*	**
H	−6.92	−6.90	ΔE_{H-L}	5.66	5.08	6.92	6.90	1.26	1.83	2.83	2.54	4.09	4.36	−4.09	−4.36	0.35	0.39	2.95	3.75
L	−1.26	−1.83																	
H-1	−7.87	−6.97	$\Delta E_{H-1-L_{+1}}$	7.38	5.33	7.87	6.97	0.49	1.63	3.69	2.67	4.18	4.30	−4.18	−4.30	0.27	0.37	2.36	3.47
L + 1	−0.49	−1.63																	
H-2	−8.30	−6.99	$\Delta E_{H-2-L_{+2}}$	9.36	6.18	8.30	6.99	−1.06	0.81	4.68	3.09	3.62	3.90	−3.62	−3.90	0.21	0.32	1.40	2.46
L + 2	1.06	−0.81																	

H: HOMO (Highest Occupied Molecular Orbital), L: LUMO (Lowest Unoccupied molecular orbital), eV: electron volt, $(eV)^{-1}$: 1/electron volt.
*EIMC ligand.
**$[Ag(EIMC)_2]ClO_4$ complex.

7.59, the theoretical value was calculated at 7.67 ppm. The experimental value for the H3/H3i atoms of the synthesized Ag(I) complex was recorded at 7.72 ppm, while the theoretical value was found at 7.78/7.74 ppm. In the experimental spectrum of the free ligand, chemical shift values for H8 and H6/H7 atoms were assigned at 1.36 and 1.39 ppm. The theoretical values corresponding to these atoms are 1.33 and 1.48 ppm, respectively. The chemical shift values for the H6/H6i, H7/H7i, and H8/H8i atoms of the complex were observed at 1.36 ppm. Theoretical values were calculated as 1.36 ppm for H8/H8i and 1.51 ppm for the others. For H1 and H2 atoms, the peaks were observed at 8.26 and 7.09 in the ^{1}H NMR spectrum of the EIMC ligand and were found to be 8.32 and 7.23 ppm in the theoretical spectrum. The chemical shift values of H1/H1i and H2/H2i atoms for the synthesized $[Ag(EIMC)_2]ClO_4$ complex were also observed at 8.45 and 7.15 ppm and calculated at 9.18/9.54 and 8.02/7.30 ppm.

The shift of the recorded experimental values of the free ligand H1 and H2 atoms to higher values in the spectrum of the synthesized complex indicates that the complexation is correct. The obtained results show that these two atoms interact with the oxygen atoms of the perchlorate, and the structure is analyzed correctly.

For C6, C5, C4, C3, C2, and C1 atoms of the EIMC ligand, chemical shift values of the carbon atoms were recorded at 14.42, 64.71, 148.79, 117.80, 130.67, and 137.54 ppm and calculated at 13.97, 69.05, 156.44, 122.69, 136.27, and 143.43 ppm. The chemical shift values of C6/C6i, C5/C5i, C4/C4i, C3/C3i, C2/C2i, and C1/C1i atoms for the title complex were recorded at 13.96, 64.22, 147.52, 117.31, 129.85, and 137.84 ppm in the experimental spectrum, and no significant shift was observed with respect to the free ligand. The theoretical values were found to be 13.96, 69.94/70.09, 155.41/155.87, 123.39/122.64, 136.33/138.13, and 149.94/144.12 ppm, respectively.

3.5. Molecular orbital descriptor analysis

The HOMO and LUMO molecular orbitals represent the ability of an organic or inorganic molecule to donate and take electrons. The gap in energy levels among these molecular orbitals is a crucial factor in determining the reactivity, hardness, and overall behavior of molecules. Also, the value of this energy gap is a feature that also impacts optical polarizability. Soft molecules have a lower energy need for excitation, making them more susceptible to polarization compared to hard molecules [68–70]. The HOMO and LUMO energies, along with other quantum chemical property values, of the EIMC ligand and $[Ag(EIMC)_2]ClO_4$ complex were presented in Table 6. In calculations performed in the gas phase, the energy values of the HOMO and LUMO orbitals were found to be −6.92 and −1.26 eV for the EIMC ligand and −6.90 and −1.83 eV for the $Ag(EIMC)_2ClO_4$ complex, respectively. The energy gap value for the free ligand was calculated at 5.66 eV, while the energy gap value for the synthesized complex was calculated at 5.08 eV. The HOMO-LUMO energy gap value of the $[Ag(EIMC)_2]ClO_4$ complex is slightly smaller than the EIMC ligand. For the EIMC ligand and its Ag(I) complex, global hardness values were found to be 2.83 and 2.54 eV, respectively. Also, global softness values were calculated at 0.35 and 0.39 eV. The chemical potential values are −4.09 eV and −4.36 eV. Since the chemical hardness values are much greater than the chemical softness values and the chemical potential values are negative, both structures have low reactivity and a tendency to enter chemical reactions. Since the energy gap of the synthesized complex is not significantly lower than that of the free ligand, lower energy is required for its excitation.

Fig. 4 displays the HOMO and LUMO molecular orbital distributions in the gas phase of the EIMC ligand and $[Ag(EIMC)_2]ClO_4$ complex.

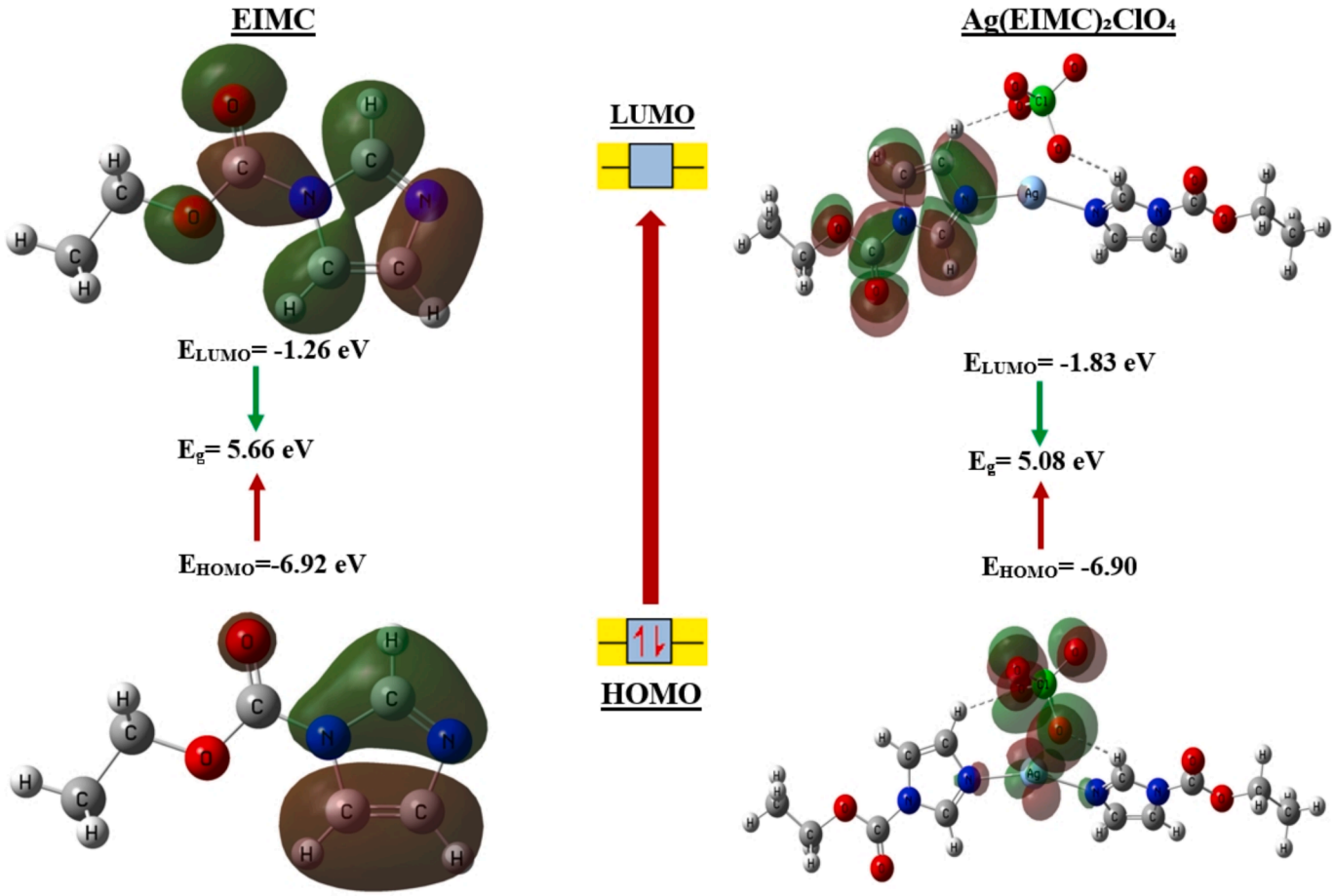

Fig. 4. HOMO and LUMO plots of the EIMC ligand and the $[Ag(EIMC)_2]ClO_4$ complex in the gas phase.

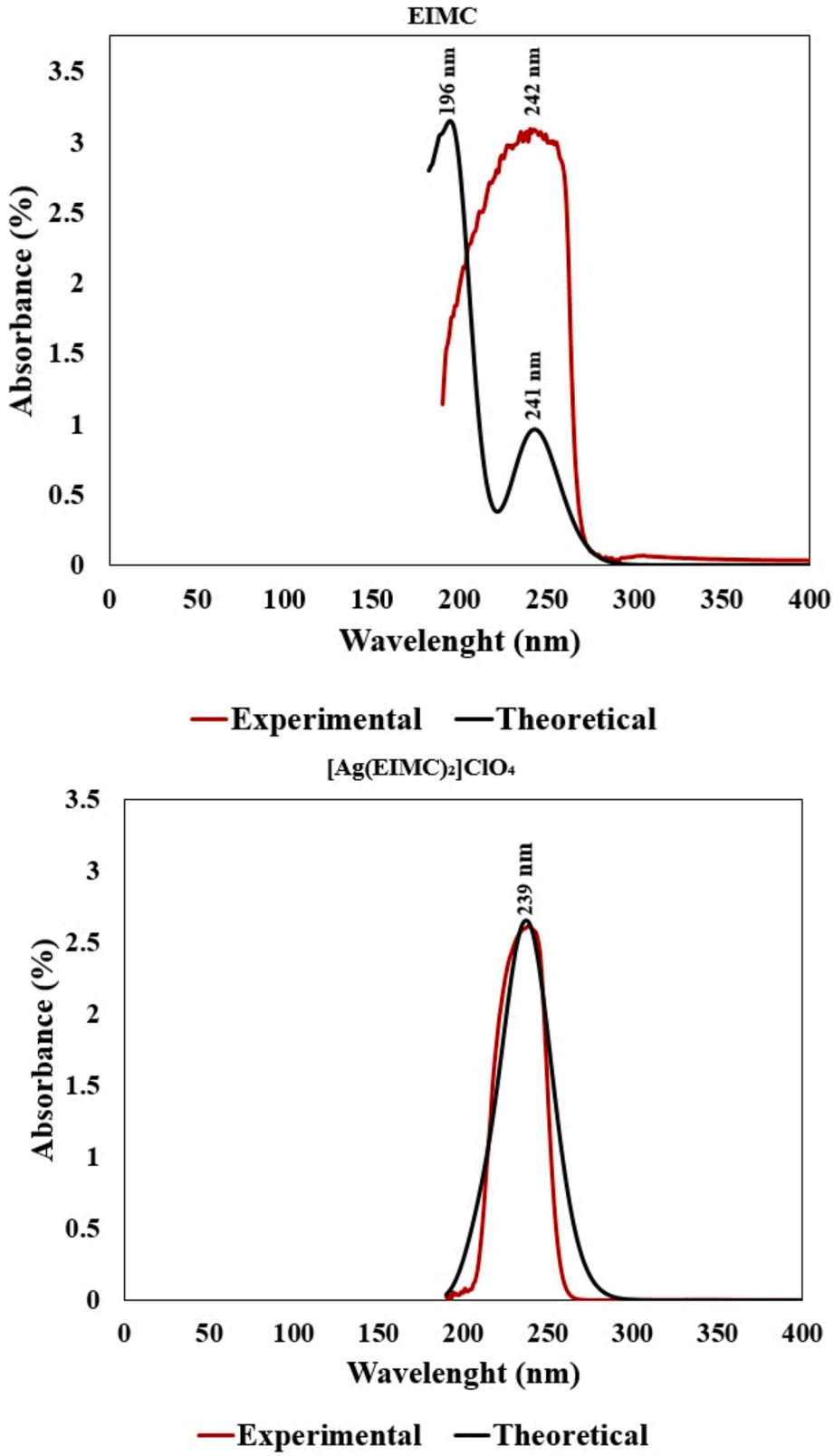

Fig. 5. Experimental and theoretical UV–Vis spectra of the EIMC ligand and the $[Ag(EIMC)_2]ClO_4$ complex.

These maps use the color red to represent the positive phase and the color green to represent the negative phase [71].

In the HOMO maps of the EIMC ligand, negative regions are distributed on the N atoms of the imidazole ring. When a charge transition occurs to the LUMO orbital, they are distributed on the oxygen atoms of the carboxylate group. For the synthesized Ag(I) complex, the charge distribution in the HOMO orbital is concentrated on Cl_4O_4, while as a result of the charge transfer to the LUMO orbital, the charge distribution is concentrated on the imidazole ring. The negative regions in the HOMO orbital are the O atoms of ClO_4.

Table 7
Experimental and theoretical UV–Vis parameters of the EIMC ligand and the $[Ag(EIMC)_2]ClO_4$ complex.

Molecule	Experimental	Theoretical				
	λ (nm)	λ (nm)	E (eV)	f	Symmetry	Major Contributions
EIMC	242	241	5.70	0.0759	Singlet-A	HOMO → LUMO
$Ag(EIMC)_2ClO_4$	-	196	6.30	0.2157	Singlet-A	HOMO-2 → LUMO
	239	239	5.16	0.0933	Singlet-A	HOMO-1 → LUMO
						HOMO-2 → LUMO

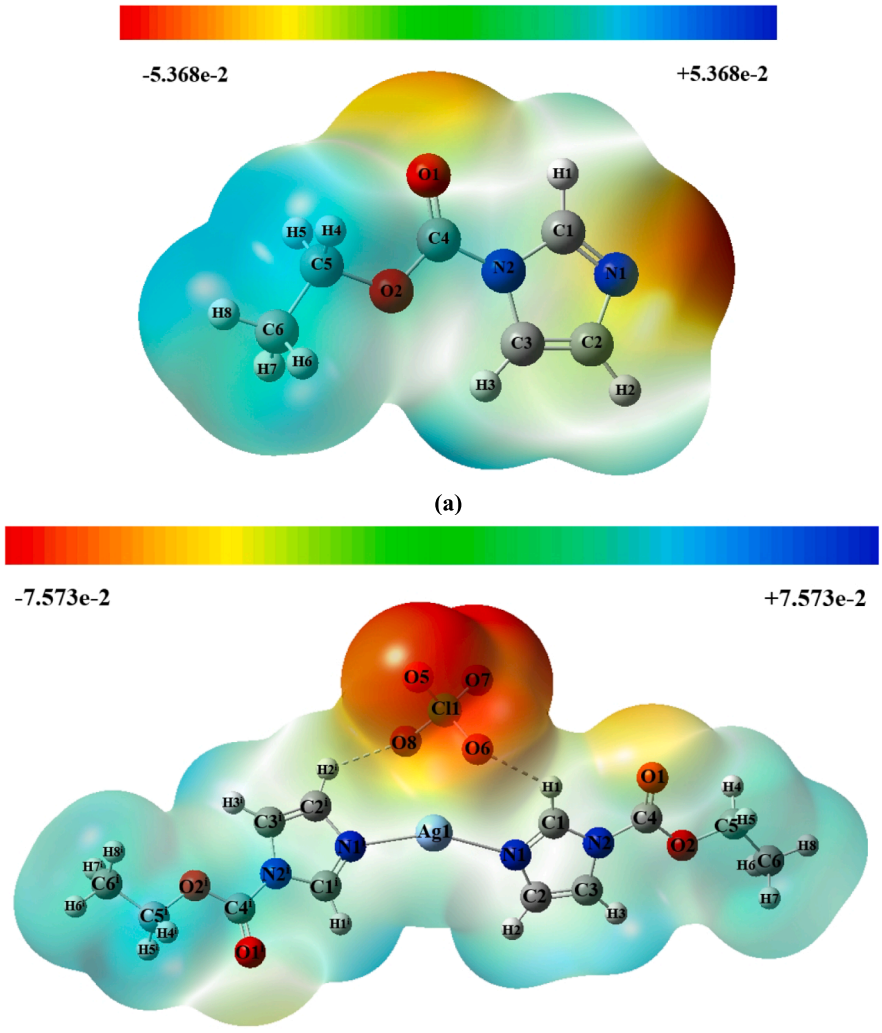

(a)

(b)

Fig. 6. MEPs of the EIMC ligand (**a**) and the $[Ag(EIMC)_2]ClO_4$ complex (**b**) in the gas phase.

3.6. UV–Vis spectrum analysis

Experimental and theoretical methods were used to perform the UV–Vis spectrum analysis of the EIMC ligand and $[Ag(EIMC)_2]ClO_4$ complex. The UV–Vis spectra were experimentally recorded in water solvent. The UV–Vis spectra were presented in Fig. 5, and the corresponding peak values were listed in Table 7. The computed findings indicate that the EIMC molecule exhibits signals at 196 and 241 nm wavelengths in the electronic absorption spectrum. In response to the signal originating from the HOMO → LUMO transition calculated at 241 nm and with an oscillator power of 0.0759, the experimental value was observed at a wavelength of 242 nm. In the recorded and calculated electronic absorption spectrum of the $[Ag(EIMC)_2]ClO_4$ complex, a signal was observed at 239 nm, which is due to the HOMO-1 → LUMO and HOMO-2 → LUMO transitions with an oscillator strength of 0.0933. These wavelengths in the UV–Vis spectra come from the π → π * electronic transition.

3.7. Molecular electrostatic potential surface map (MEP) analysis

The molecular electrostatic potential surface map is a tool used to identify the electrophilic and nucleophilic areas of a molecule based on a color scale that follows the order red < orange < yellow < green < blue. In this map, the red and blue colors represent electron-rich and electron-

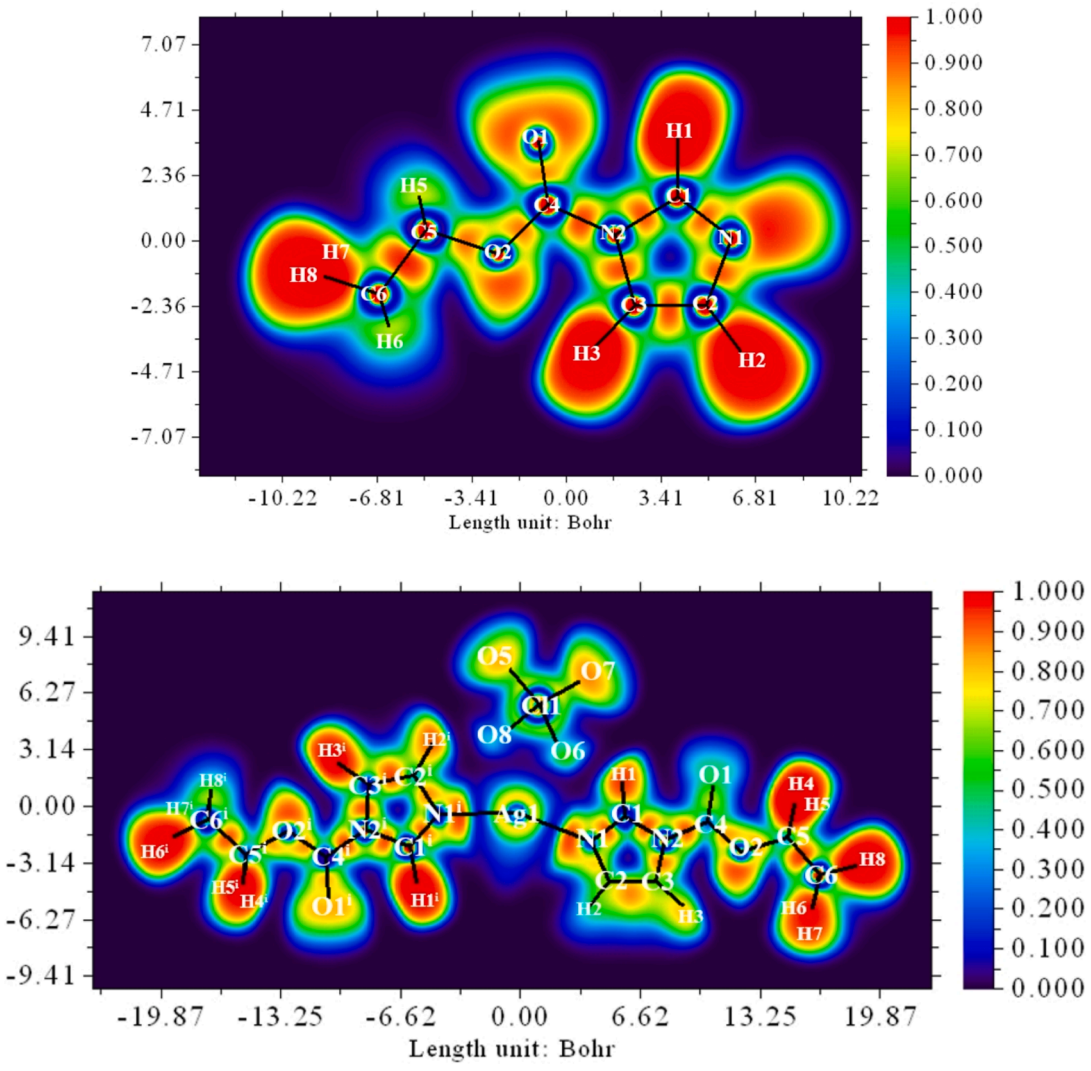

(a)

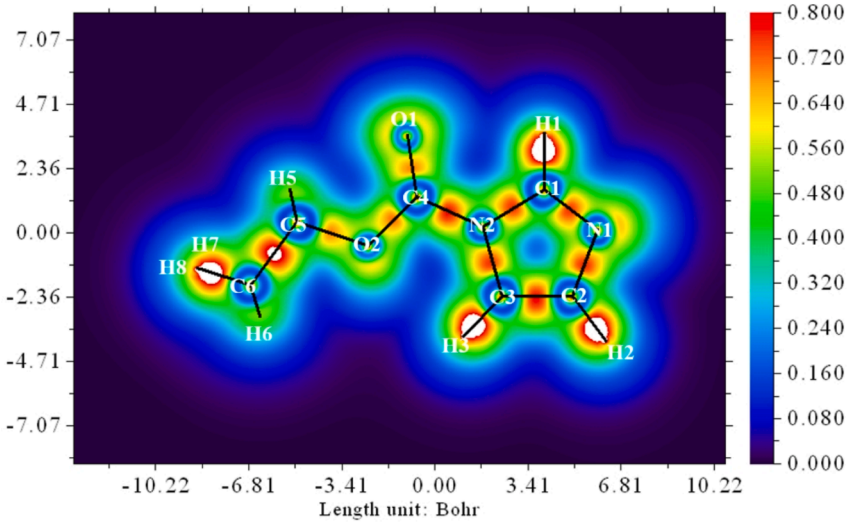

Fig. 7. ELF (a) and LOL (b) maps the EIMC ligand and the $[Ag(EIMC)_2]ClO_4$ complex.

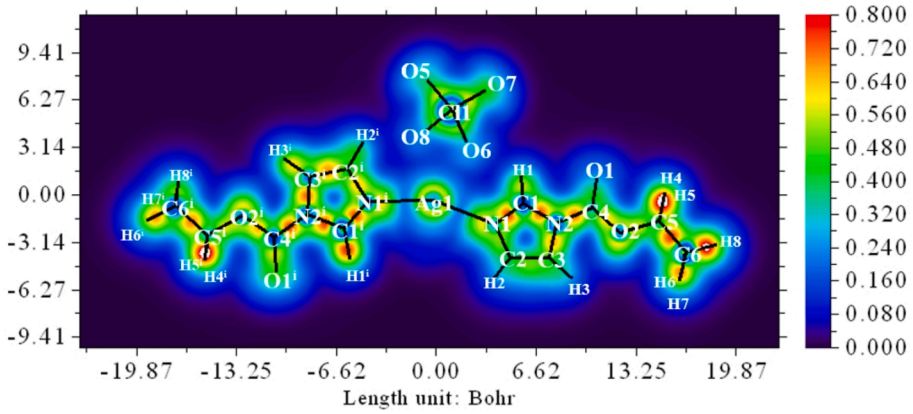

(b)

Fig. 7. (*continued*).

poor regions, respectively. The yellow exhibits less negative regions than the red. The green color shows neutral regions [72,73]. The created MEP maps for the optimized geometric structures of the EIMC molecule in the gas phase and the water solvent are given in Fig. 6.

For the calculations in the gas phase, the most negative value of the electron density of the EIMC ligand is −0.05365 a.u., and the most positive value is + 0.05365 a.u.. These two values are −0.07573 a.u. and + 0.07573a.u. for the map of the $[Ag(EIMC)_2]ClO_4$ complex. In the map designed for the EIMC ligand, electron-rich, that is, electrophilic regions were found to be the N1 atom of the imidazole ring and the O1 atom of the carboxylate group. Also, all other atoms were almost found to be in the nucleophilic region. When the map of the synthesized complex is examined, since the N1 and $N1^i$ atoms of the imidazole ring of the EIMC ligand are coordinated with the Ag atom, the charge value of these atoms is positive, and the electrophilic regions are concentrated on the O atoms of ClO_4. In other words, when the synthesized structure enters a chemical reaction, the nucleophilic attack will be on the O atoms of ClO_4.

3.8. ELF and LOL analysis

ELF and LOL are the topological analysis methods used to identify the chemical properties of a molecule, such as molecular bonding, chemical shell structure, and lone pair electrons in compounds. ELF describes the electron pair density in a structure. In contrast, LOL defines maximum localized orbitals that overlap due to the inclination of the orbitals. Both methods allow a similar interpretation of chemical properties depending on kinetic energy density [74]. The limit values for the ELF map are 0.00 and 1.00, while for the LOL map they are 0.00 and 0.80. In these maps, red and blue colors indicate regions with high and low ELF and LOL values, respectively. Namely, delocalized electrons are specified in this map below 0.5, while bound and unbound localized electrons are defined in the range between 0.5 and 1.00 [75].

When the ELF maps designed for the EIMC ligand and $[Ag(EIMC)_2]ClO_4$ complex in Fig. 7 are examined, the H atoms of the molecule are in the red-colored region, and there are bound and unbound localized electrons on these atoms. The blue ring appearing around the nitrogen and carbon atoms of the imidazole ring, the oxygen and carbon atoms of the carboxylate group, and the carbon atoms of the ethyl group also indicates that delocalized electrons are concentrated on these atoms. In addition, there is a blue ring around the silver atom and the Cl atom of the perchlorate group, and the O5 and O7 atoms are in the yellow region. The white color appearing around the H atoms in the LOL map of the ligand means that the 0.08 limit has been exceeded. According to the LOL map of the ligand, delocalized electrons are concentrated on C, N, and O atoms. The LOL map of the complex also gave results similar to those of the ELF map.

3.9. APT, Hirshfeld, and NBO charge analysis

Three different charge analyses were performed to confirm and support the data regarding the electrophilic (negative) and nucleophilic (positive) regions obtained from the MEP maps prepared for the gas phase of the EIMC ligand and $[Ag(EIMC)_2]ClO_4$ complex [76]. The calculated charge values are presented in Supplementary Table S1. When the APT, Hirshfeld, and NBO charge analysis results of the EIMC ligand were examined, the atoms with the most negative values were found to be O1, O2, N1, and N2. APT, Hirshfeld, and NBO charge values for the O1 atom are −0.806, −0.281, and −0.596, and −0.479, −0.206, and −0.474 for the N1 atom. The APT, Hirshfeld, and NBO charges for O1 of the synthesized complex are −0.771, −0.248, and −0.567, while the charge values for the N1 atom are −0.519, −0.248, and −0.567, respectively. The charge values of the calculated $O1^i$ atom are −0.810, −0.265, and −0.589, and −0.566, −0.113, and −0.567 for the $N1^i$ atom, respectively. According to the MEP map of the free ligand, the O1 and N1 atoms were the most electrophilic in this molecule during any reaction. Especially the results obtained from the Hirshfeld and NBO charge analyses confirm this data. However, the most negative atoms of the $[Ag(EIMC)_2]ClO_4$ complex were found to be O atoms of the perchlorate group. The most positive atoms in the complex are the Cl1 and Ag1 atoms. The APT, Hirshfeld, and NBO charge values were calculated as 2.454, 0.608, and 2.362 for the Cl1 atom and 0.872, 0.271, and 0.733 for the Ag1 atom. The data obtained from the charge analysis of the synthesized complex was also found to be quite consistent with its MEP map. The calculations were very useful in correctly determining the electrophilic and nucleophilic regions of both the free ligand and the synthesized complex.

3.10. Fukui function analysis

Condensed Fukui functions are one of the important tools used to investigate a molecule's reactive fields for nucleophilic, electrophilic, and radical attacks at a constant potential [77]. Fukui functions were calculated using the following [78]:

$$f_k^- = q_k(N) - q_k(N-1) \text{ electrophilic attack} \quad (1)$$

$$f_k^+ = q_k(N+1) - q_k(N) \text{ nucleophilic attack} \quad (2)$$

$$f_k^0 = (1/2)[q_k(N+1) - q_k(N-1)] \text{ neutral attack} \quad (3)$$

The value of qk represents the total charge at the rth atom. Additionally, qkN, qk(N + 1), and qk(N-1) are the charges in the neutral,

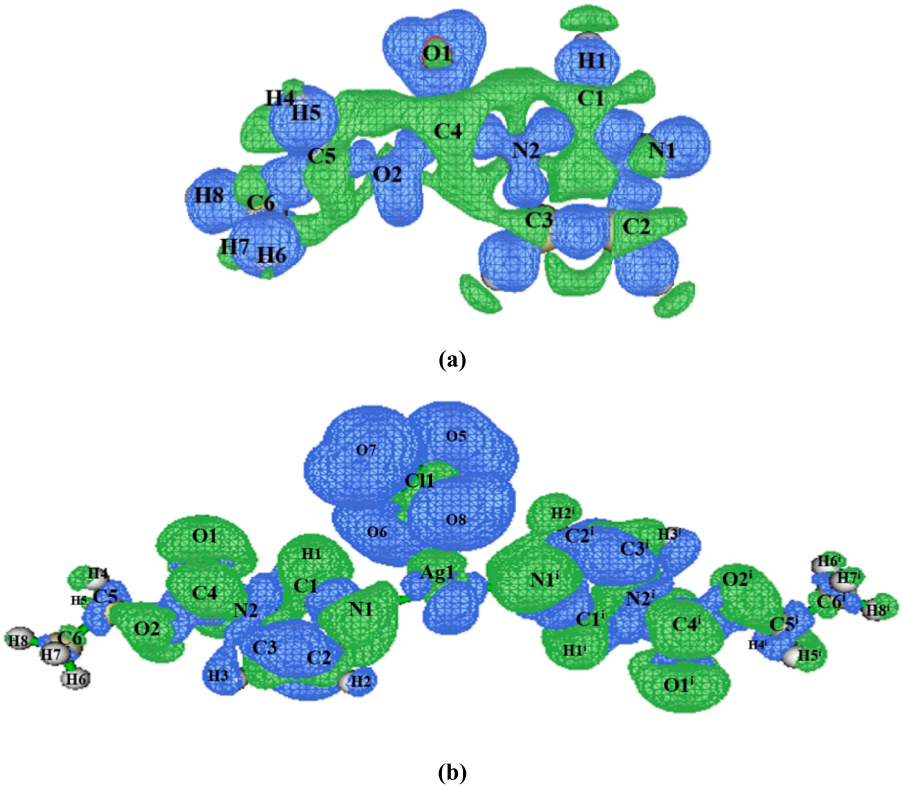

Fig. 8. Dual descriptor images of the EIMC ligand **(a)** and the $[Ag(EIMC)_2]ClO_4$ complex **(b)**.

anionic, and cationic forms of the molecule. The dual descriptors obtained by applying the formula (4) to the Fukui functions offer distinct discernment between nucleophilic and electrophilic reactions inside a molecule or complex [78,79].

$$\Delta f(r) = f^{+}(r) - f^{-}(r) \tag{4}$$

The Fukui function values for the EIMC ligand and the $[Ag(EIMC)_2]ClO_4$ complex are listed in Supplementary Table S2. At the same time, the dual descriptor images created by the Multiwfn program are also given in Fig. 8. In these maps, blue regions represent electrophilic areas, which are prone to nucleophilic assaults, while green parts represent nucleophilic areas, which are favorable for electrophilic attacks.

In the synthesized complex, the blue-colored regions are mostly concentrated on the O atoms of the perchlorate group. In other words, these atoms show electrophilic properties during any reaction. In the $[Ag(EIMC)_2]ClO_4$ complex, oxygen and nitrogen atoms are in the green-colored region and show nucleophilic properties. These results are also parallel to the data obtained from the Gaussian program and presented in Supplementary Table S2. In addition, the results obtained from the Fukui functions are quite compatible with the results obtained from the MEP map and charge analyses.

3.11. Hirshfeld surface analysis

Using the CrystalExplorer 17 software program, Hirshfeld surface analysis and associated two-dimensional fingerprint drawings were carried out to examine the contributions of various intermolecular interactions in the crystal packing motif [41]. Fig. 9 displays Hirshfeld surface analysis maps created using the d_{norm}, d_i, and d_e characteristics. The distances between a specific location on the surface and the closest atoms inside and outside are d_e and d_i. The function of these normalized distances is used to map the Hirshfeld surfaces across the norm. Short connections, intermolecular distances equivalent to van der Waals radii, and longer contacts are indicated by the red, white, and blue hues used for dnorm-mapped Hirshfeld surfaces [80,81]. The more prominent interactions between oxygen and hydrogen (O–H) atoms are shown by the red area on the dnorm Hirshfeld map, whereas other visible spots on the Hirshfeld surface represent the H-H or other connections.

The blue spikes on the lower left and right with the middle part of the fingerprint plots in Fig. 10 indicate that the O···H/H···O (47.1 %) interactions contribute the most to the Hirshfeld surfaces. Under the O–H areas are H···H/H···H (34.4 %) interactions, and the other highest contribution to the Hirshfeld surfaces comes from this interaction.

3.12. Reduced density gradient (RDG) analysis

Reduced density gradient (RDG) analysis is one of the most effective methods used to investigate and evaluate the non-covalent interactions of a molecule [82]. An approach was designed by van der Walls, Johnson et al. to identify and visualize the weak interactions of a molecule, including hydrogen bonding and steric effects [83]. This method can be considered as a representation of a fundamental dimensionless quantity in DFT calculations that characterizes the electron distribution deviation [84]. The graph presenting the nature of intramolecular and intermolecular interactions was designed for the Ag (I) complex and is presented in Fig. 11. In this graph, blue, green, and red colors represent hydrogen bond interaction, van der Waals interactions, and steric interactions, respectively [85]. The red colors observed in the center of the imidazole rings of the complex structure are related to π-π stacking interactions and represent steric interactions. Van der Waals interactions are between the H1 and $H2^i$ atoms of the imidazole rings and the O6 and O8 atoms of the perchlorate.

3.13. Biological activity results

3.13.1. Antioxidant activity

The antioxidant activities of ligand (EIMC), complex $[Ag(EIMC)_2]ClO_4$, and standard (ascorbic acid) substances were determined by

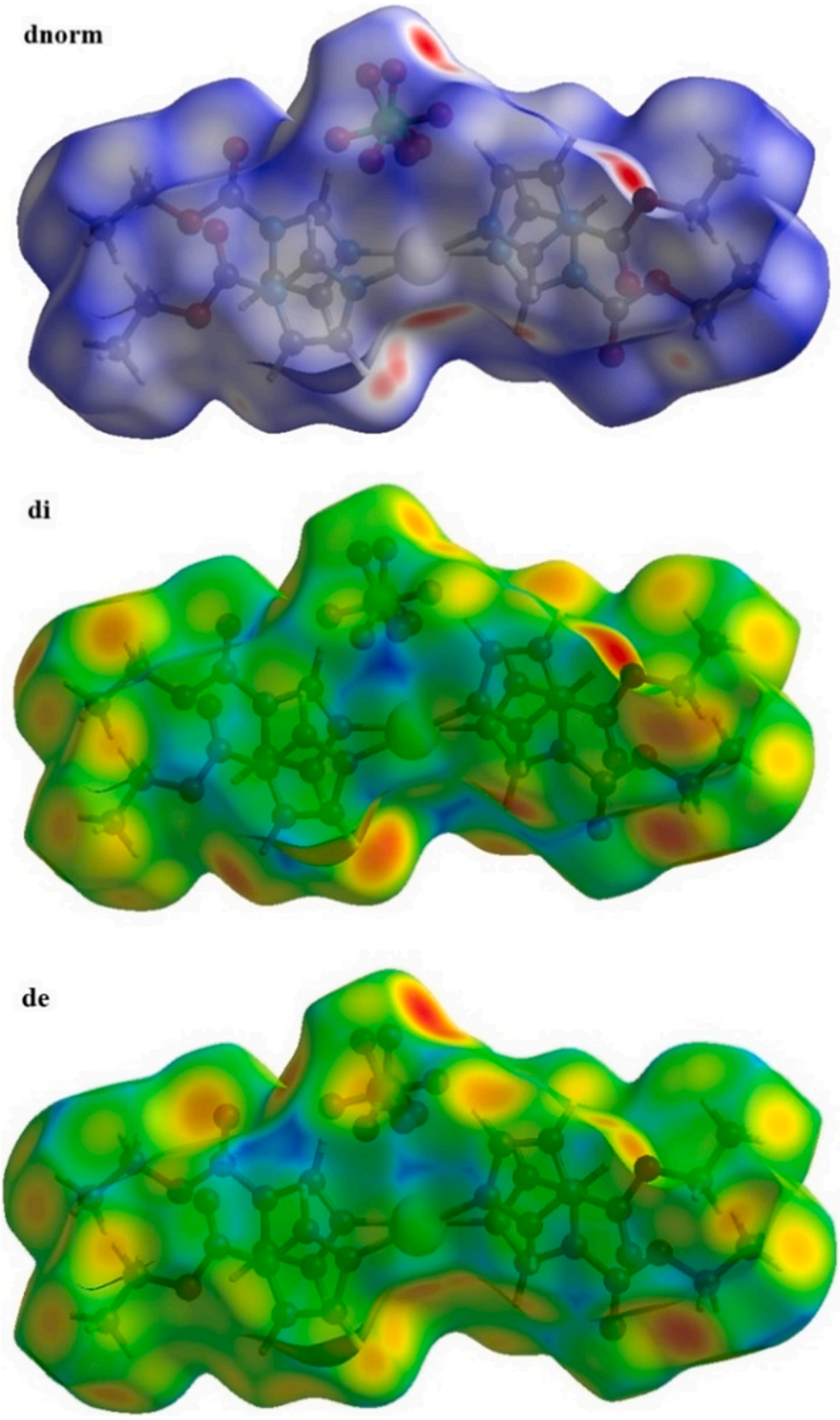

Fig. 9. The Hirshfeld surface maps of the $[Ag(EIMC)_2]ClO_4$ mapped over d_{norm}, d_i and d_e.

investigating the ability of these substances to inhibit $ABTS^{\bullet+}$ and $DPPH^{\bullet}$ radicals. Samples of each sample to be examined were prepared at three different concentrations (25, 50, and 100 μg/mL). The percentages of inhibition of both radicals and IC_{50} values of these prepared samples were determined. The results are shown in Table 8 and Fig. 12.

The amount of antioxidant substance required to scavenge 50 % of the radical concentration in the samples is called the IC_{50} value. The smaller the IC_{50} value, the higher the antioxidant activity [86,87]. Two different radicals were used in the antioxidant activity analyses of the ligand and silver complex in the study, and the results were compared with standard ascorbic acid results. Since $ABTS^{\bullet+}$ radicals are well dissolved in inorganic and water solvents, they are used especially in the determination of antioxidant activities of hydrophilic and lipophilic substances [88]. $ABTS^{\bullet+}$ radical IC_{50} values of the samples were determined as ligand (123.84 μg/mL), complex (173.79 μg/mL), and standard ascorbic acid (16.33 μg/mL), respectively. The $DPPH^{\bullet}$ radical

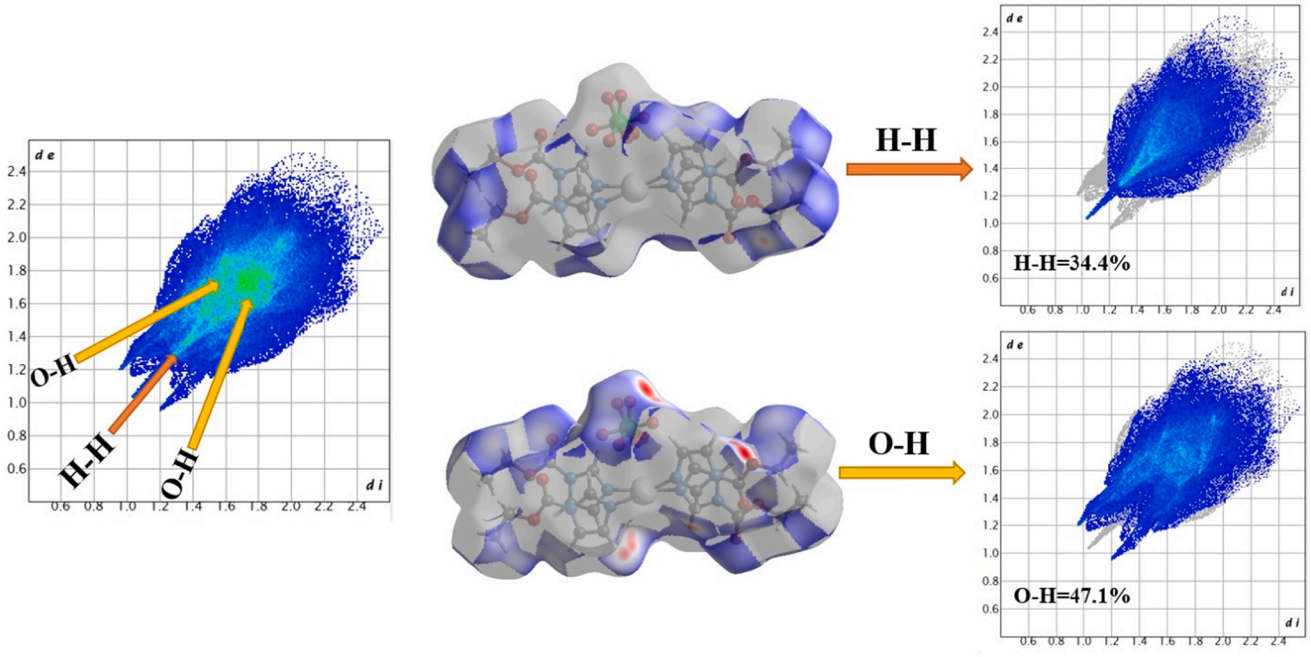

Fig. 10. 2D fingerprint plots order with a dnorm view of the O···H/H···O(47.1%), H···H/ H···H (34.4%), contacts in the $[Ag(EIMC)_2]ClO_4$.

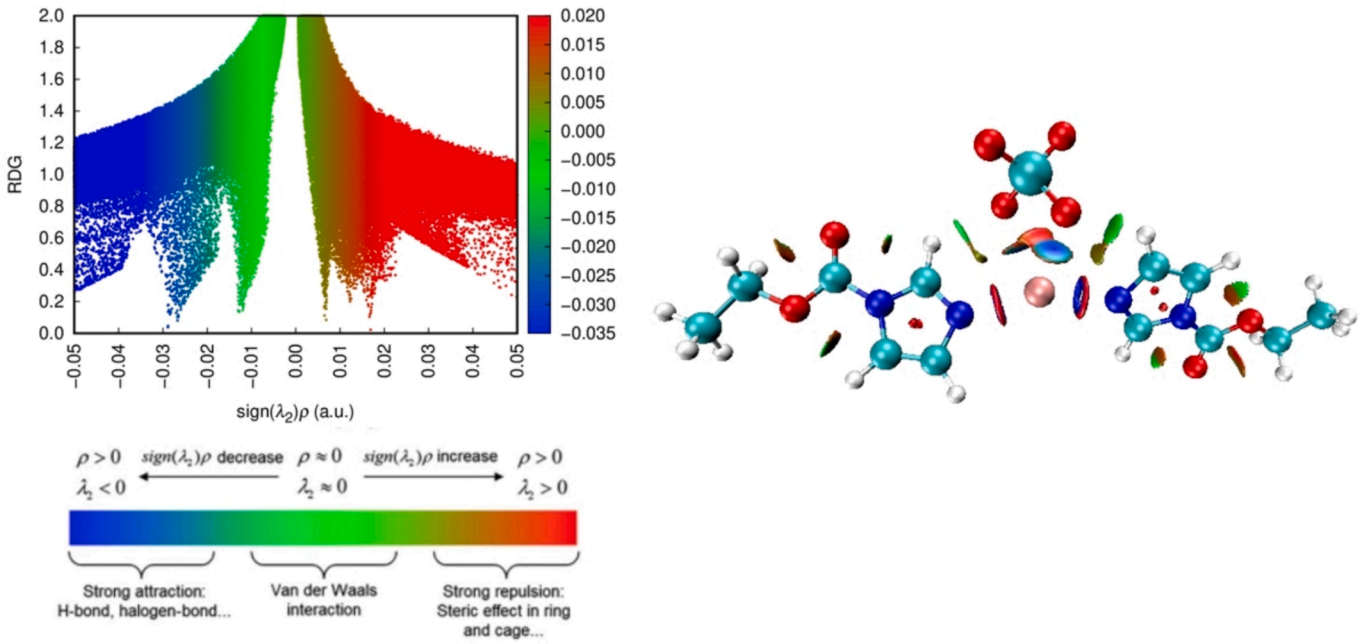

Fig. 11. 2D scattering and isosurface intensity plots showing the non-bonded interactions of the $[Ag(EIMC)_2]ClO_4$ complex.

easily reacts with lipophilic, hydrophilic, and weak antioxidants. Therefore, it is frequently used in antioxidant capacity studies [89]. The DPPH$^{\bullet}$ radical scavenging IC_{50} values of the ligand, complex, and standard ascorbic acid in the study were determined as 103.36, 162.64, and 11.94 μg/mL, respectively. The radical scavenging activity results of the samples show that these substances inhibit both radicals, and especially their inhibition of the DPPH$^{\bullet}$ radical is higher. In addition, it was determined that the inhibition power of these two radicals of the ligand was greater than that of the silver complex. In a study on 2,4,5-trisubstituted imidazole derivatives, the antioxidant activity of these substances was determined. For this purpose, ABTS$^{\bullet+}$ and DPPH$^{\bullet}$ radicals were used, and as a result of this study, it was determined that the ABTS$^{\bullet+}$ radical IC_{50} values varied between 0.162 ± 0.006 mg/mL and 42.158 ± 2.697 mg/mL, and the DPPH$^{\bullet}$ radical IC_{50} values varied between 0.141 ± 0.094 mg/mL and 16.89 ± 0.636 mg/mL [90]. In another study, the antioxidant activities of 1H-benzo[d]imidazole-5-carboxamide derivatives were investigated, and it was concluded that the DPPH$^{\bullet}$ radical IC_{50} values varied between 72.14 ± 0.21 μM and 115.36 ± 1.16 μM [91]. Studies have shown that imidazole-containing substances have significant antioxidant properties [92]. It was determined that our results were compatible with the studies in the literature.

3.13.2. Antidiabetic activity

α-amylase and α-glucosidase enzymes play an important role in

Table 8
Radicals inhibition percentages and IC_{50} values of the EIMC ligand, the [Ag $(EIMC)_2]ClO_4$ complex, and standard ascorbic acid.

Samples	Concentration (μg/mL)	% inhibition ($ABTS^{\bullet+}$)	IC_{50} (μg/mL)	% inhibition ($DPPH^{\bullet}$)	IC_{50} (μg/mL)
Ligand (EIMC)	25	23.21 ± 1.34	123.84	24.93 ± 1.44	103.36
	50	32.37 ± 1.40		36.95 ± 1.38	
	100	43.26 ± 1.32		48.08 ± 1.36	
Complex [Ag $(EIMC)_2]ClO_4$	25	10.19 ± 1.48	173.79	15.22 ± 1.36	162.64
	50	19.22 ± 1.36		25.07 ± 1.40	
	100	30.25 ± 1.31		34.10 ± 1.38	
Standard (Ascorbic acid)	25	51.93 ± 1.34	16.33	53.16 ± 1.36	11.94
	50	64.43 ± 1.40		66.28 ± 1.43	
	100	80.42 ± 1.31		81.31 ± 1.45	

accelerating the decomposition and absorption of carbohydrates into the bloodstream. Therefore, they are in a regulatory position in the control of diabetes. In particular, α-amylase hydrolyzes α-1,4-glycosidic bonds in carbohydrates and breaks them into smaller oligo- and disaccharide units. On the other hand, α-glucosidase enzyme breaks down the degraded carbohydrates into glucose [93,94]. It is important to find and develop new antidiabetic drugs with less toxic effects that inhibit the enzymes α-amylase and α-glucosidase. The inhibition percentages of both enzymes (α-amylase and α-glucosidase) and IC_{50} values of the ligand, silver complex, and standard drug acarbose substances in the study were calculated. Three different concentrations of the samples, 25, 50, and 100 mg/mL, were studied. The results are shown in Table 9 and Fig. 13.

When the α-glucosidase enzyme IC_{50} values of the ligand, silver complex, and standard drug acarbose samples were examined, it was determined that they were 161.64, 156.12, and 27.66 μg/mL, respectively. In addition, the IC_{50} values of α-amylase enzyme were determined as 165.19, 158.30, and 30.94 μg/mL, respectively. The α-glucosidase enzyme inhibition of twenty-three synthesized carbazole–imidazole derivatives was investigated. It was reported that the IC_{50} values of these synthesized substances ranged from 74.0 ± 0.7 to 298.3 ± 0.9 μM and that they had stronger inhibitory effects than standard acarbose [95].

In another study, it was reported that the α-glucosidase enzyme IC50 values of twenty-four synthesized imidazole-thiadiazole compounds varied between 1.4 ± 0.01 and 13.6 ± 0.01 μM, and the α-amylase enzyme IC50 values varied between 0.9 ± 0.01 and 12.8 ± 0.02 μM [96]. When our study results were compared with the studies in the literature, it was determined that our ligand and silver complex inhibited α-glucosidase and α-amylase enzymes. In particular, it was determined that the α-glucosidase enzyme inhibition of the samples was higher than the α-amylase enzyme inhibition. In addition, when compared with standard acarbose, it can be said that the silver complex has a moderate antidiabetic capacity.

4. Conclusion

In this study, the structural and spectroscopic properties of the EIMC

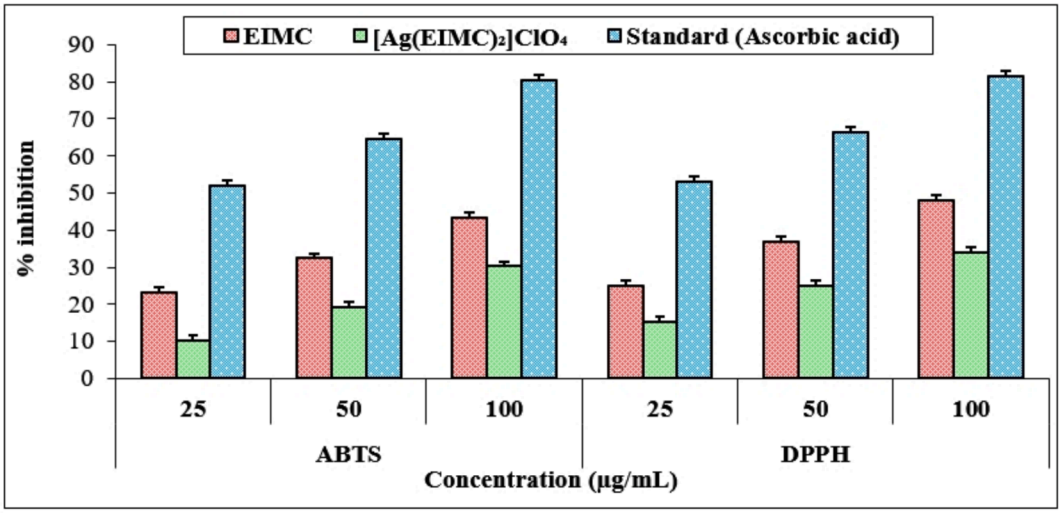

Fig. 12. Radical inhibition percentages of EIMC ligand, the $[Ag(EIMC)_2]ClO_4$ complex, and standard.

Table 9
α-glucosidase and α-amylase enzyme inhibition percentages with IC_{50} values of the EIMC ligand, the $[Ag(EIMC)_2]ClO_4$ complex, and standard acarbose.

Samples	Concentration (μg/mL)	% inhibition (α-glucosidase)	IC_{50} (μg/mL)	% inhibition (α-amylase)	IC_{50} (μg/mL)
Ligand (EIMC)	25	17.61 ± 1.36	161.64	16.78 ± 1.32	165.19
	50	28.30 ± 1.25		25.39 ± 1.23	
	100	35.29 ± 1.17		34.51 ± 1.40	
Complex $[Ag(EIMC)_2]ClO_4$	25	23.57 ± 1.22	156.12	19.51 ± 1.28	158.30
	50	30.81 ± 1.43		28.29 ± 1.41	
	100	38.62 ± 1.37		36.58 ± 1.47	
Standard (Acarbose)	25	47.10 ± 1.34	27.66	46.32 ± 1.22	30.94
	50	60.33 ± 1.42		58.81 ± 1.36	
	100	72.56 ± 1.36		71.53 ± 1.40	

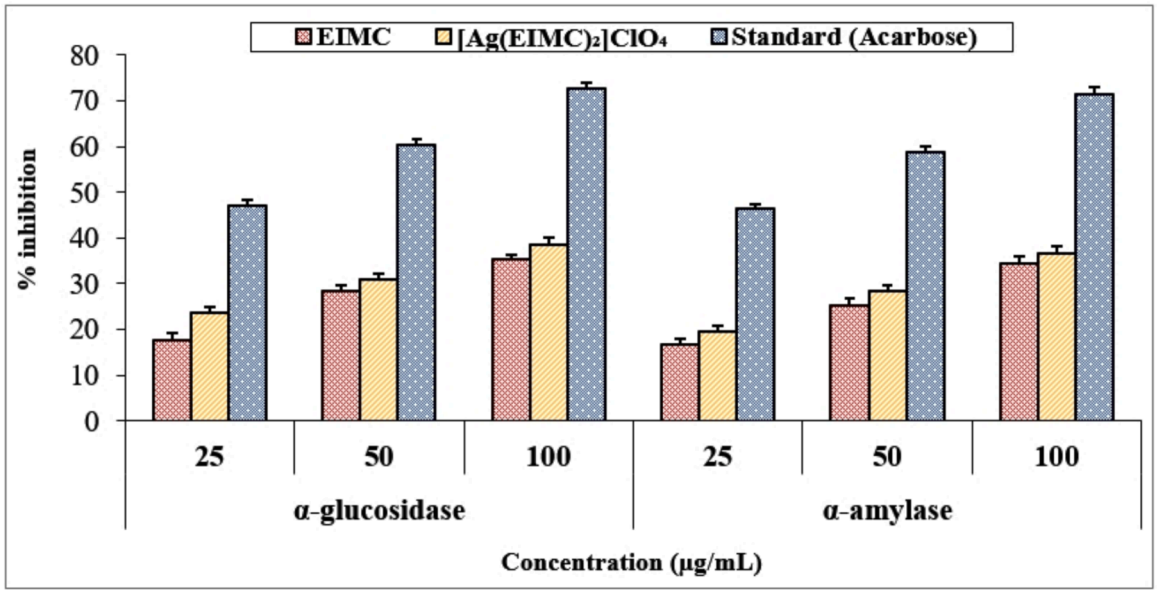

Fig. 13. α-glucosidase and α-amylase enzyme inhibition percentages of the EIMC ligand, the $[Ag(EIMC)_2]ClO_4$ complex and standard.

ligand and the its Ag(I) complex synthesized from it were investigated by experimental and theoretical calculation methods and compared with each other, and it was seen that the results were quite compatible. The electronic properties of both structures were investigated in the gas phase. According to these results, it was determined that these two molecules have a low tendency to enter into chemical reactions and a high tendency to remain stable. MEP, ELF, and LOL maps were designed, and the electronic properties were evaluated by calculating the charge values and Fukui functions. As a result of this study, it was determined that the most active site for the EIMC ligand was the N1 atom, and in the synthesized complex, the Ag atom reacted with the N1 atom. In the synthesized complex, the oxygen atoms of the perchlorate group were found in the atoms with the highest negative value. As a result, the electrophilic and nucleophilic regions of these two structures were determined in detail with all the calculation methods for electronic properties. The ligand had a greater inhibition and the IC50 values of the α-glucosidase and α-amylase enzymes were close to one another when the radical scavenging action of the title compounds whose biological activity was researched was examined. It was also determined that the α-glucosidase enzyme activity was higher than the α-amylase enzyme activity. It was concluded that the silver complex had stronger antidiabetic activity than the ligand. When the results were compared with the standard drug acarbose, it could be said that the complex and the ligand had moderate antidiabetic properties. Finally, in vitro analyses were performed to determine the antioxidant, α-glucosidase, and α-amylase activities of both structures, and extremely significant biological activity values were obtained.

CRediT authorship contribution statement

Ceyhun Kucuk: Writing – original draft, Visualization, Validation, Supervision, Software, Methodology, Investigation, Conceptualization. **Meltem Erdem-Kucuk:** Writing – original draft, Visualization, Supervision, Methodology, Investigation, Conceptualization. **Ebru Coteli:** Writing – original draft, Visualization, Supervision, Methodology, Investigation, Conceptualization. **Sibel Celik:** Writing – original draft, Visualization, Supervision, Software, Methodology, Investigation, Conceptualization. **Namık Özdemir:** Writing – original draft, Visualization, Software, Methodology, Investigation, Conceptualization.

Declaration of competing interest

The authors declare that they have no known competing financial interests or personal relationships that could have appeared to influence the work reported in this paper.

Appendix A. Supplementary data

Supplementary data to this article can be found online at https://doi.org/10.1016/j.inoche.2025.114876.

Data availability

No data was used for the research described in the article.

References

[1] S. Verma, D.S. Joshi, Imidazole: having versatile biological activities, J. Chemist. (2013) 329412, https://doi.org/10.1155/2013/329412.
[2] A.M. Vijesh, A.M. Isloor, S. Telkar, S.K. Peethambar, S. Rai, N. Isloor, Synthesis, characterization and antimicrobial studies of some new pyrazole incorporated imidazole derivatives, Eur. J. Med. Chem. 46 (2011) 3531–3556, https://doi.org/10.1016/j.ejmech.2011.05. 005.
[3] B. Narasimhan, D. Sharma, P. Kumar, Biological importance of imidazole nucleus in the new millennium, Med. Chem. Res. 20 (2011) 1119–1140, https://doi.org/10.1007/s00044-010-9472-5.
[4] G. Teli, P.A. Chawla, Hybridization of imidazole with Various heterocycles in Targeting cancer: a decade's work, Chemistryslect 6 (19) (2021) 4803–4836, https://doi.org/10.1002/slct.202101038.
[5] K. Shalini, P.K. Sharma, N. Kumar, Imidazole and its biological activities: a review, Der Chem. Sinica 1 (3) (2010) 36–47.
[6] J. Pandey, V.K. Tiwari, S.S. Verma, V. Chaturvedi, S. Bhatnagar, S. Sinha, A. N. Gaikwad, R.P. Tripathi, Synthesis and antitubercular screening of imidazole derivatives, Eur. J. Med. Chem. 44 (2009) 3350–3355, https://doi.org/10.1016/j.ejmech.2009.02.013.
[7] M. Boiani, M. González, Imidazole and benzimidazole derivatives as chemotherapeutic agents, mini-reviews, Med. Chem. 5 (2005) 409–424, https://doi.org/10.2174/1389557053544047.
[8] A.R. Spasov, I.N. Iezhitsa, L.I. Bugaeva, V.A. Anisimova, Benzimidazole derivatives: Spectrum of pharmacological activity and toxicological properties (a review), Khim. Farm. Zhurn. 33 (1999) 6–17, https://doi.org/10.1007/BF02510042.
[9] L. Sim, K. Jayakanthan, S. Mohan, R. Nasi, B.D. Johnston, B.M. Pinto, D.R. Rose, New glucosidase inhibitors from an ayurvedic herbal treatment for type 2 diabetes: structures and inhibition of human intestinal maltase-glucoamylase with compounds from Salacia reticulate, Biochemistry 3 (2010) 443, https://doi.org/10.1021/bi9016457.
[10] J.K. Grover, S. Yadav, V. Vats, Medicinal plants of India with anti-diabetic potential, J. Ethnopharmacol. 1 (2002) 81–100, https://doi.org/10.1016/S0378-8741(02) 00059-4.

[11] V.S. Suvith, D. Philip, Catalytic degradation of methylene blue using biosynthesized gold and silver nanoparticles, pectrochim, Acta - A: Mol. Biomol. 118 (2014) 526–532, https://doi.org/10.1016/j.saa.2013.09.016.

[12] S. Navalon, A. Dhakshinamoorthy, M. Alvaro, H. Garcia, Metal nanoparticles supported on two-dimensional graphenes as heterogeneous catalysts, Coord. Chem. Rev. 312 (2016) 99–148, https://doi.org/10.1016/j.ccr.2015.12.005.

[13] A. Kedziora, M. Speruda, E. Krzyzewska, J. Rybka, A. Łukowiak, G. Bugla-Płoskońska, Similarities and differences between silver ions and silver in nanoforms as antibacterial agents, Int. J. Mol. Sci. 19 (2) (2018) 444, https://doi.org/10.3390/ijms19020444.

[14] L. Panacek, R. Kvitek, M. Prucek, R. Kolar, N. Vecerova, V.K. Pizurova, T. J. Sharma, R. Nevecn, Zboril, silver colloid nanoparticles: synthesis, characterization, and their antibacterial activity, J. Phys. Chem. B 110 (33) (2006) 16248–16253, https://doi.org/10.1021/jp063826h.

[15] A. Thati, R. Noble, B.S. Rowan, M. Creaven, M. Walsh, D. McCann, K. Egan, Kavanagh, mechanism of action of coumarin and silver (I)–coumarin complexes against the pathogenic yeast *Candida albicans*, Toxicol in Vitro 21 (5) (2007) 801–808, https://doi.org/10.1016/j.tiv.2007.01.022.

[16] B.S. Creaven, D.A. Egan, K. Kavanagh, M. McCann, M. Mahon, A. Noble, B. Thati, M. Walsh, Synthesis and antimicrobial activity of copper(II) and silver(I) complexes of hydroxynitrocoumarins: x-ray crystal structures of $[Cu(hnc)_2(H_2O)_2] \bullet 2H_2O$ and [Ag(hnc)] (hncH = 4-hydroxy-3-nitro-2H-chromen-2-one), Polyhedron 24 (2005) 949–957, https://doi.org/10.1016/j.poly.2005.03.006.

[17] M. Baia, L. Baia, W. Kiefer, J. Popp, Surface-enhanced raman scattering and density functional theoretical study of anthranil adsorbed on colloidal silver particles, J. Phys. Chem. B 108 (45) (2004) 17491–17496, https://doi.org/10.1021/jp047899h.

[18] S. Günal, N. Kaloglu, I. Ozdemir, S. Demir, I. Ozdemir, Novel benzimidazolium salts and their silver complexes: synthesis and antibacterial properties, Inorg. Chem. Commun. 21 (2012) 142–146, https://doi.org/10.1016/j.inoche.2012.04.033.

[19] N.S. Abdel-Kader, S.A. Abdel-Latif, A.L. El-Ansary, M.A. Hemeda, Design, synthesis, spectroscopic studies, DFT, TD-DFT/ PCM calculations, and molecular docking studies on the anti-SARS and anti-COVID-19 activities of novel benzidine bis azo 1-(2-Hydroxy-3-naphthoic acid) complexes with some transition metal ions, Polycyclic Aromat. Compd. 44 (6) (2023) 3601–3632, https://doi.org/10.1080/10406638.2023.2237629.

[20] T. Murugan, R. Venkatesh, K. Geetha, A. Abdou, Synthesis, spectral investigation, DFT, antibacterial, antifungal and molecular docking studies of Ni(II), Zn(II), Cd(II) complexes of tetradentate schiff-base ligand, Asian J. Chem. 35 (6) (2023) 1509, https://doi.org/10.14233/ajchem.2023.27808.

[21] M. Valko, D. Leibfritz, J. Moncol, M.T.D. Cronin, M. Mazur, J. Telser, Free radicals and antioxidants in normal physiological functions and human disease, Int J Biochem Cell Biol. 39 (2007) 44–84, https://doi.org/10.1016/j.biocel.2006.07.001.

[22] W.W. Nawar, Lipids, in: O.R. Fennema (Ed.), Food Chemistry, 3rd ed., Marcel Dekker, New York, 1996, pp. 225–319.

[23] J.S. Johansen, A.K. Harris, D.J. Rychly, A. Ergul, Oxidative stress and the use of antioxidants in diabetes: linking basic science to clinical practice, Cardiovasc Diabetol. 4 (2005) 5, https://doi.org/10.1186/1475-2840-4-5.

[24] F.A. Matough, S.B. Budin, Z.A. Hamid, N. Alwahaibi, J. Mohamed, The role of oxidative stress and antioxidants in diabetic complications, Sultan Qaboos Univ. Med. J. 12 (1) (2012) 5–18, https://doi.org/10.12816/0003082.

[25] S.D.M. Bandeira, L.J.S. da Fonseca, G.D.S. Guedes, L.A. Rabelo, M.O.F. Goulart, S. M.L. Vasconcelos, Oxidative stress as an underlying contributor in the development of chronic complications in diabetes mellitus, Int. J. Mol. Sci. 14 (2) (2013) 3265–3284, https://doi.org/10.3390/ijms14023265.

[26] S.Wild, G. Roglic, A. Green, R. Sicree, H. King Global prevalence of diabetes: estimates for the year 2000 and projections for 2030. Diabetes Care, 27 (5) (2004) 1047–1053. Doi: 10.2337/diacare.27.5.1047.

[27] S.M. Grundy, A constellation of complications: the metabolic syndrome, Clin. Cornerstone 7 (2005) 36–45, https://doi.org/10.1016/S1098-3597(05)80066-3.

[28] R.R.O. Andrade, J.C.S. Salgado, G.N. Vázquez, S.P. Webster, M. Binnie, S. G. Jiménez, I.L. Rivera, P.C. Vázquez, R.V. Molina, S.E. Soto, Antidiabetic and toxicological evaluations of naringenin in normoglycaemic and NIDDM rat models and its implicationson extra-pancreatic glucose regulation, diabetes, Obes. Metab. 10 (2008) 1097–1104, https://doi.org/10.1111/j.1463-1326.2008.00869.x.

[29] S. Seshasai, S. Kaptoge, A. Thompson, E. DiAngelantonio, P. Gao, N. Sarwar, P. H. Whincup, K.J. Mukamal, R.F. Gillum, I. Holme, I. Njølstad, Diabetes mellitus, fasting glucose, and risk of cause-specific death, N. Engl. J. Med. 364 (2011) 829–841, https://doi.org/10.1056/NEJMoa1008862.

[30] N. Dege, H. Gökce, O.E. Doğan, G. Alpaslan, T. Ağar, S. Muthu, Y. Sert, Quantum computational, spectroscopic investigations on N-(2-((2-chloro-4,5-dicyanophenyl) amino)ethyl)-4-methylbenzenesulfonamide by DFT/TD-DFT with different solvents, molecular docking and drug-likeness researches, Colloids Surf. A Physicochem. Eng. Asp. 638 (2022) 128311, https://doi.org/10.1016/j.colsurfa.2022.128311.

[31] Y.S. Mary, Y.S. Mary, S. Armakovic, S.J. Armakovic, R. Yadav, I. Celik, P. Mane, B. Chakraborty, Stability and reactivity study of bio-molecules brucine and colchicine towards electrophile and nucleophile attacks: insight from DFT and MD simulations, J. Mol. Liq. 335 (2021) 116192, https://doi.org/10.1016/j.molliq.2021.116192.

[32] P.K. Murthy, V. Suneetha, S. Armaković, P.A. Suchetan, L. Giri, R.S. Rao, Synthesis, characterization and computational study of the newly synthetized sulfonamide molecule, J. Mol. Struct. 1153 (2018) 212–229, https://doi.org/10.1016/j.molstruc.2017.10.028.

[33] M.J. Frisch, G.W. Trucks, H.B. Schlegel, G.E. Scuseria, M.A. Robb, J.R. Cheeseman, G. Scalmani, V. Barone, G.A. Petersson, H. Nakatsuji, X. Li, M. Caricato, A.V. Marenich, J. Bloino, B.G. Janesko, R. Gomperts, B. Mennucci, H.P. Hratchian, J.V. Ortiz, A.F. Izmaylov, J.L. Sonnenberg, D. WilliamsYoung, F. Ding, F. Lipparini, F. Egidi, J. Goings, B. Peng, A. Petrone, T. Henderson, D. Ranasinghe, V.G. Zakrzewski, J. Gao, N. Rega, G. Zheng, W. Liang, M. Hada, M. Ehara, K. Toyota, R. Fukuda, J. Hasegawa, M. Ishida, T. Nakajima, Y. Honda, O. Kitao, H. Nakai, T. Vreven, K. Throssell, J.A. Montgomery Jr, J.E. Peralta, F. Ogliaro, M.J. Bearpark, J. J. Heyd, E.N. Brothers, K.N. Kudin, V.N. Staroverov, T.A. Keith, R. Kobayashi, J. Normand, K. Raghavachari, A.P. Rendell, J.C. Burant, S.S. Iyengar, J. Tomasi, J.M. Cossi Millam, M. Klene, C. Adamo, R. Cammi, J.W. Ochterski, R.L. Martin, K. Morokuma, O. Farkas, J.B. Foresman and D.J. Fox, Gaussian, Inc., Wallingford CT, 2016.

[34] R. Dennington, T.A. Keith, J.M. Millam, GaussView, Version 6.1. Shawnee Mission (KS), Semichem Inc, 2016.

[35] A.D. Becke, Density-functional thermochemistry III. the role of exact exchanege, J. Chem. Phys. 98 (1993) 5648–5652.

[36] S. Celik, M. Alp, S. Yurdakul, A combined experimental and theoretical study on vibrational spectra of 3-pyridyl methyl ketone, Spectrosc. Lett 53 (4) (2020) 234–248.

[37] K. Subashini, S. Periandy, Spectroscopic (FT-IR, FT-raman, UV, NMR, NBO) investigation and molecular docking study of (R)- 2-Amino-1-PhenylEthanol, J. Mol. Struct. 1117 (2016) 240–256.

[38] C. Kucuk, S. Yurdakul, N. Özdemir, B. Erdem, Crystal structure, vibrational spectroscopy, 1H NMR, and DFT analyses with antibacterial activity studies on silver nitrate complex of 5-iodoindole, Inorg. Chem. Commun. 150 (2023) 110465.

[39] L.E.H. Paul, I.C. Foehn, A. Schwarzer, E. Brendler, U. Bohme, ¨salicylaldehyde-(2-hydroxyethyl)imine – a flexible ligand for group 13 and 14 elementsSalicylaldehyde-(2-hydroxyethyl)imine – a flexible ligand for group 13 and 14 elements, Inorganica. Chim. Acta. 423 (A) (2014) 268–280.

[40] H.B. Howsaui, A.S. Basaleh, M.H. Abdellattif, W.M.I. Hassan, M.A. Hussien, Synthesis, structural investigations, molecular docking, and anticancer activity of some novel schiff bases and their uranyl complexes, Biomolecules 11 (8) (2021) 1138, https://doi.org/10.3390/biom11081138.

[41] B. Silvi, A. Savin, Classification of chemical bonds based on topological analysis of electron localization functions, Nature 371 (6499) (1994) 683–686.

[42] P.R. Spackman, M.J. Turner, J.J. McKinnon, S.K. Wolff, D.J. Grimwood, D. Jayatilaka, M.A. Spackman, CrystalExplorer: a program for hirshfeld surface analysis, visualization and quantitative analysis of molecular crystalsCrystalExplorer: a program for hirshfeld surface analysis, visualization and quantitative analysis of molecular crystals, J. Appl. Cryst. 54 (3) (2021) 1006–1011.

[43] Y.E. Bakiri, M. Kurbanova, A.Ahsin, F. Gurbanova, M. Ashfaq, O. Şahin, M.N. Tahir, A. Qamar, H.A. Abuelizz, R. Al-Salahi, Single crystal XRD, Hirshfeld surface analysis and computational approach for exploration of novel xanthene derivative, J. Mol. Struct.

[44] K.V. Sarayu Jayadevan, A.R. Sujithc, Biju, Crystal structure, hirshfeld surface analysis and DFT studies of 2-[4-(2-methyl-prop-yl)phen-yl]-N′-[(1Z)-1-(thio-phen-2-yl)ethyl--idene]propane-hydrazide, Acta Crystallogr. E. 81 (5) (2025) 417–419.

[45] C.A. Rice-Evans, Screening of phenolics and flavonoids for antioxidant activity, Academic Press, Elsevier, 1999, pp. 239–253.

[46] M.S. Blois, Antioxidant determinations by the use of a stable free radical, Nature 181 (1958) 1199–1200, https://doi.org/10.1038/1811199a0.

[47] Y.I. Kwon, E. Apostolidis, K. Shetty, Inhibitory potential of wine and tea aganist aamylase and aglucosidase for management of hyperglycemia linked to type 2 diabetes, J. Food Biochem. 32 (2008) 15–31, https://doi.org/10.1111/j.1745-4514.2007.00165.x.

[48] E. Apostolidis, Y.I. Kwon, K. Shetty, Inhibitory potential of herb, fruit, and fungalenriched cheese against key enzymes linked to type 2 diabetes and hypertension, Innov. Food Sci. Emerg. Technol. 8 (2007) 46–54, https://doi.org/10.1016/j.ifset.2006.06.001.

[49] Bruker APEX2 and SAINT 2013 Bruker AXS Inc. Madison, Wisconsin, USA.

[50] G.M. Sheldrick, *SHELXT – integrated space-group and crystal-structure determination*, Acta Cryst. A 71 (1) (2015) 3–8, https://doi.org/10.1107/S2053273314026370.

[51] G.M. Sheldrick, *Crystal structure refinement with SHELXL*, Acta Cryst. C 71 (1) (2015) 3–8, https://doi.org/10.1107/S2053229614024218.

[52] O.V. Dolomanov, L.J. Bourhis, R.J. Gildea, J.A.K. Howard, H. Puschmann, *OLEX2: a complete structure solution, refinement and analysis program*, J. Appl. Cryst. 42 (2) (2009) 339–341, https://doi.org/10.1107/S0021889808042726.

[53] A. Bondi, *van der waals volumes and radii*, J. Phys. Chem. 68 (3) (1964) 441–451, https://doi.org/10.1021/j100785a001.

[54] S. Gatfaoui, N. Issaoui, S.A. Brandan, T. Roisnel, H. Marouani, Synthesis and characterization of p-xylylenediaminium bis(nitrate). effects of the coordination modes of nitrate groups on their structural and vibrational properties, J. Mol. Struct. 1151 (2018) 152–168.

[55] T. Sundius, S.A. Brandan, Structural, harmonic force field and vibrational studies of cholinesterase inhibitor tacrine used for treatment of Alzheimer's disease, Heliyon 9 (2023) e717280.

[56] M. Govindarajan, K. Ganasan, S. Periandy, M. Karabacak, S. Mohan, Vibrational spectroscopic analysis of 2-chlorotoluene and 2-bromotoluene: a combined experimental and theoretical study, Spectrochim. Acta A 77 (5) (2010) 1005–1013, https://doi.org/10.1016/j.saa.2010.08.038.

[57] M.H. Jamroz Vibrational energy distribution analysis (VEDA): scopes and limiations. specrochim acta a 114 2004 10.1016/j.saa.2013.05.096 220 230.

[58] Y. Erdoğdu, M.T. Gulluoglu, S. Yurdakul, O. Dereli, DFT simulations, FT-IR, FT-raman, and FT-NMR spectra of 4-(4-chlorophenyl)-1H-imidazole molecules, Opt. Spectrosc. 113 (1) (2012) 23–32.
[59] M. Arivazhagan, S. Manivel, S. Jeyavijayan, R. Meenakshi, Vibrational spectroscopic (FTIR and FT-raman), first-order hyperpolarizablity, HOMO, LUMO, NBO, mulliken charge analyses of 2-ethylimidazole based on Hartree–Fock and DFT calculations, Spectrochim Acta A 134 (2015) 493–501, https://doi.org/10.1016/j.saa.2014.06.108.
[60] Y. Erdogdu, D.M.T. Güllüoglu, S. Yurdakul, O. Dereli, DFT simulations, FT-IR, FT-raman, and FT-NMR spectra of 4-(4-chlorophenyl)-1H-imidazole molecules, Opt. Spect. 113 (1) (2012) 23–32.
[61] R.M. Silverstein, F.X. Webster, D.J. Kiemle, D.l., Bryce spectrometric identification of organic compounds, John Wiley & Sons, Singapore, 2014.
[62] V. Sathyanarayanmoorthi, R. Karunathan, V. Kannappan, Molecular modeling and spectroscopic studies of benzothiazole, J. Chem. (2013) 258519, https://doi.org/10.1155/2013/258519.
[63] H. Arslan, Ö. Algül, Theoretical studies of Molecular structure and vibrational spectra of 2-ethyl-1H-benzo[d]imidazole, Asian J. Chem. 19 (3) (2007) 2229–2235.
[64] A. Atac, M. Karabacak, C. Karaca, E. Kose, NMR, UV, FT-IR, FT-raman spectra and molecular structure (monomeric and dimeric structures) investigation of nicotinic acid N-oxide: a combined experimental and theoretical study, Spectrochim Acta A 85 (2012) 145–154, https://doi.org/10.1016/j.saa.2011.09.048.
[65] M. Karabacak, Z. Calisir, M. Kurt, E. Kose, A. Atac, The spectroscopic (FT-IR, FT-raman, dispersive raman and NMR) study of ethyl-6-chloronicotinate molecule by combined density functional theory, Spectrochim Acta 153 (2016) 754–770, https://doi.org/10.1016/j.saa.2015.09.007.
[66] M.T. Bilkan, S. Yurdakul, Experimental and theoretical studies on Molecular structures and vibrational modes of novel compounds containing Silver1, Russ. J. Inorg. Chem. 62 (7) (2017) 910–924.
[67] S. Uzun, Z. Esen, E. Koç, N.C. Usta, M. Ceylan, Experimental and density functional theory (MEP, FMO, NLO, Fukui functions) and antibacterial activity studies on 2-amino-4-(4-nitrophenyl) -5,6-dihydrobenzo [h] quinoline-3-carbonitrile, J. Mol. Struct. 1178 (2019) 450–457, https://doi.org/10.1016/j.molstruc.2018.10.001.
[68] A. Mahmood, A. Irfan, J.L. Wang, Machine learning for organic photovoltaic polymers: a minireview, Chin. J. Polym. Sci. 40 (2022) 870–876.
[69] A. Mahmood, M. Ali, M. Saqib, M.I. Abdullah, B. Khalid, Theoretical investigation for the designing of novel antioxidants, Can. J. Chem. 91 (2) (2013) 126–130, https://doi.org/10.1139/cjc-2012-0356.
[70] S. Celik, DFT investigations and molecular docking as potent inhibitors of SARS-CoV-2 main protease of 4-phenylpyrimidine, J. Mol. Struct. 1277 (2023) 134895, https://doi.org/10.1016/j.molstruc.2022.134895.
[71] R. Balu, A.R. Ayub, A. Panneerselvam, M.S. Devi, J.R. Rajabathar, H. Al-Lohedan, G. Devendrapandi, Growth, experimental and theoretical investigation on the nonlinear optical, vibrational, and electronic properties of L–2–aminobutyric acid D–methionine crystal: a combined experimental and quantum chemical approach, J. Mater. Sci.: Mater. Electron. 35 (2024) 874, https://doi.org/10.1007/s10854-024-12622-4.
[72] S. Kumar, A. Radha, M. Kour, R. Kumar, A. Chouaih, S.K. Pandey, DFT studies of disubstituted diphenyldithiophosphates of nickel(II): structural and some spectral parameters, J. Mol. Struct. 1185 (2019) 212–218, https://doi.org/10.1016/j.molstruc.2019. 02.105.
[73] M.A. Mumita, T.K. Pala, M.A. Alam, A.A.M. Islama, S. Paulb, M.C. Sheikh, DFT studies on vibrational and electronic spectra, HOMO–LUMO, MEP, HOMA, NBO and molecular docking analysis of benzyl-3N-(2,4,5-trimethoxyphenylmethylene) hydrazinecarbodithioate, J. Mol. Struct. 1220 (2020) 128715, https://doi.org/10.1016/j.molstruc.2020.128715.
[74] T. Manickavelu, B. Govindrajan, M. Sambantham, P. Panneerselvam, A. Irfan, Computational investigation, effects of polar and non-polar solvents on optimized structure with topological parameters (ELF, LOL, AIM, and RDG) of three glycine derivative compounds, Struct. Chem. 33 (2022) 1295–1319, https://doi.org/10.1007/s11224-022-01930-2.
[75] M. Vennila, R. Rathikha, S. Muthu, A. Jeelani, A. Irfan, Theoretical structural analysis (FT-IR, FT-R), solvent effect on electronic parameters NLO, FMO, NBO, MEP, UV (IEFPCM model), Fukui function evaluation with pharmacological analysis on methyl nicotinate, Comput. Theo. Chem. 1217 (2022) 113890, https://doi.org/10.1016/j.comptc.2022.113890.
[76] S. Yurdakul, E. Temel, O. Buyukgungor, (Crystal structure, spectroscopic characterization, thermal properties and theoretical investigations on [Ag(methyl 4-pyridylketone)2NO3], J. Mol. Struct. 1191 (2019) 301–313, https://doi.org/10.1016/j.molstruc.2019. 04.071.
[77] F. Akman, Effect of solvents on intra- and inter-molecular interactions of oligothiophenes, J. Mol. Model. 29 (2023) 276.
[78] B. Raajaraman, N.R. Sheela, S., Muthu spectroscopic, quantum computational and molecular docking studies on 1-phenylcyclopentane carboxylic acid, Comput. Biol. Chem. 82 (2019) 44–56, https://doi.org/10.1016/j.compbiolchem.2019.05.011.C.
[79] A. Morell, A. Grand, Toro-labbe new dual descriptor for chemical reactivity, J. Phys. Chem. A. 109 (2005) 205e212, https://doi.org/10.1021/jp046577a.
[80] S.K. Seth, Structural elucidation and contribution of intermolecular interactions in *O*-hydroxy acyl aromatics: insights from X-ray and hirshfeld surface analysis, J. Mol. Struct. 1064 (2014) 70–75.
[81] E.P. Cuadradoa, K. Ferrer, E. Osorioc, I. Brito, J. Cisterna, M. Gutiérrez, Crystal structure, hirshfeld surface analysis and DFT studies of N-(4-acetylphenyl) quinoline-3-carboxamide, J. Mol. Struct. 1246 (2021) 131162.
[82] M. Medimagh, N. Issaoui, S. Gatfaoui, S.A. Brandan, O. Al-Dossary, H. Marouani, M.J. Wojcik, Impact of non-covalent interactions on FT-IR spectrum and properties of 4-methylbenzylammonium nitrate, A DFT and Molecular Docking Study, Heliyon 7 (2021) e08204.
[83] E.R. Johnson, S. Keinan, P. Mori-Sanchez, J. Contreras-García, A.J. Cohen, W. Yang, Revealing noncovalent interactions, J. Am. Chem. Soc. 132 (2010) 6498–6506.
[84] R. Suja, A. Rathika, V.S.J. Reeda, A.A. Kumar, P. Divya, Synthesis, spectroscopic analysis (FT-IR, FT-raman, UV, NMR), non-covalent interactions (RDG, IGM) and dynamic simulation on bis(8–hydroxy quinoline) salicylate salicylic acid, J. Mol. Struct. 1310 (2024) 138231.
[85] R. Subramaniyan, R. Ramarajan, A. Ramalingam, S. Sambandam, A. Petersamy, A. R. Guerroudj, A. Chouaih, N. Boukabcha, Microwave assisted synthesis, vibrational spectra, hirshfeld surface and interaction energy, DFT, topology, in silico ADMET and molecular docking studies of 1,2-bis(4-methoxybenzylidene)hydrazine, J. Mol. Struct. 1278 (2023) 134946.
[86] J. Deng, W. Cheng, G. Yang, A novel antioxidant activity index (AAU) for natural products using the DPPH assay, Food Chem. 125 (4) (2011) 1430–1435, https://doi.org/10.1016/j.foodchem.2010.10.031.
[87] R. Scherer, H.T. Godoy, Antioxidant activity index (AAI) by the 2,2-diphenyl-1-picrylhydrazyl method, Food Chem. 112 (3) (2009) 654–658, https://doi.org/10.1016/j.foodchem.2008.06.026.
[88] M. Ozgen, R.N. Reese, A.Z. Tulio, J.C. Scheerens, A.R. Miller, Modified 2,2-azino-bis3-ethylbenzothiazoline-6-sulfonic acid (ABTS) method to measure antioxidant capacity of selected small fruits and comparison to ferric reducing antioxidant power (FRAP) and 2,2 '-diphenyl-1-picrylhydrazyl (DPPH) methods, J. Agricult. Food Chem. 54 (2006) 1151–1157, https://doi.org/10.1021/jf051960d.
[89] S.B. Kedare, R.P. Singh, Genesis and development of DPPH method of antioxidant assay, J. Food Sci. Technol. 48 (4) (2011) 412–422, https://doi.org/10.1007/s13197-011-0251-1.
[90] E. Noriega-Iribe, L. Díaz-Rubio, A. Estolano-Cobián, V.W. Barajas-Carrillo, J. M. Padrón, R. Salazar-Aranda, R. Díaz-Molina, V. García-González, R.A. Chávez-Santoscoy, D. Chávez, I. Córdova-Guerrero, In vitro and in silico screening of 2,4,5-trisubstituted imidazole derivatives as potential xanthine oxidase and acetylcholinesterase inhibitors, antioxidant, and antiproliferative agents, Appl. Sci. 10 (8) (2020) 2889, https://doi.org/10.3390/app10082889.
[91] C.E. Theodore, S.B. Benaka Prasad, K. Yogesh Kumar, M.S. Raghu, F. Alharethy, M. K. Prashanth, B.H. Jeon, Synthesis, molecular docking, enzyme inhibition and antioxidant potential of new 1H-benzo[d]imidazole-5-Carboxamide derivatives, J. Mol. Struct. 1302 (2024) 137521, https://doi.org/10.1016/j.molstruc.2024.137521.
[92] F. Ahmad, M.J. Alam, M. Alam, S. Azaz, M. Parveen, S. Park, S. Ahmad, Synthesis, spectroscopic, computational (DFT/B3LYP), AChE inhibition and antioxidant studies of imidazole derivative, J. Mol. Struct. 1151 (2018) 327–342, https://doi.org/10.1016/j.molstruc.2017.09.056.
[93] X. Min, S. Guo, Y. Lu, X. Xu, Investigation on the inhibition mechanism and binding behavior of cryptolepine to α-glucosidase and its hypoglycemic activity by multi-spectroscopic method, J. Lumin. 269 (2024) 120437, https://doi.org/10.1016/j.jlumin.2024.120437.
[94] X.Z. Wu, W.-J. Zhu, L. Lu, C.-M. Hu, Y.-Y. Zheng, X. Zhang, J. Lin, J.-Y. Wu, Z. Xiong, K. Zhang, X.-T. Xu, Synthesis and anti-α-glucosidase activity evaluation of betulinic acid derivatives, Arab. J. Chem. 16 (5) (2023) 104659, https://doi.org/10.1016/j.arabjc.2023.104659.
[95] M. Adiba, F. Peytama, R. Shourgeshtya, M. Mohammadi-Khanaposhtanib, M. Jahania, S. Imanparastc, M.A. Faramarzic, B. Larijanid, A.A. Moghadamniabe, E.N. Esfahanif, F. Bandarianf, M. Mahdavid, Design and synthesis of new fused carbazole-imidazole derivatives as antidiabetic agents: in vitro α-glucosidase inhibition, kinetic, and in silico studies, Bioorg. Med. Chem. Lett. 29 (5) (2019) 713–718, https://doi.org/10.1016/j.bmcl.2019.01.012.
[96] M. Maqbool, M. Solangi, K.M. Khan, M. Özil, N. Baltaş, U. Salar, S.S. Tariq, Z.U. Haq, M. Taha, Imidazole-thiadiazole hybrids: A multitarget de novo drug design approach, in vitro evaluation, ADME/T, and in silico studies, Arch Pharm (Weinheim), 2024 357 (9) (2024) e2400325. Doi: 10.1002/ardp.202400325.

Ceyhun Kucuk Education Research Topics Work Experience e-mail: ceyhun.kucuk@beun.edu.trphone number: +90541364677 I completed my undergraduate education at Samsun Ondokuz Mayıs University, Faculty of Artsand Sciences, Department of Physics, in 2010. I completed my master's degree at ZonguldakBülent Ecevit University, Institute of Science, Department of Nuclear Physics, and I havecompleted my doctorate at Gazi University, Institute of Science, Department of Atomic andMolecular Physics as of 2023. My research areas are the synthesis of organic and inorganic molecules, spectroscopic analysis,and DFT calculations, as well as the investigation of their biological activities. During and aftermy doctoral education, I have published in many important journals related to my field of study. I have been working as a lecturer at Zonguldak Bülent Ecevit University since 2017